Paradoxical Rules of Spike Train Decoding Revealed at the Sensitivity Limit of Vision

Graphical Abstract

Highlights

- Single-photon detection was resolved from retinal circuits to behavior

- Behavioral decisions rely only on the retinal ON pathway at the sensitivity limit

- Behavior does not rely on the more sensitive spike code provided by the OFF pathway

- Photon detection is driven only by information encoded as increased spiking activity

Authors

Lina Smeds, Daisuke Takeshita, Tuomas Turunen, ..., Nataliia Martyniuk, Aarni Seppänen, Petri Ala-Laurila

Correspondence

petri.ala-laurila@helsinki.fi

In Brief

Smeds et al. combine retinal ganglion cell recordings with markerless tracking of mouse behavior in photon detection. They show that behavior relies on information presented as increased spiking activity rather than the spike code carrying the maximal information.

CellPress

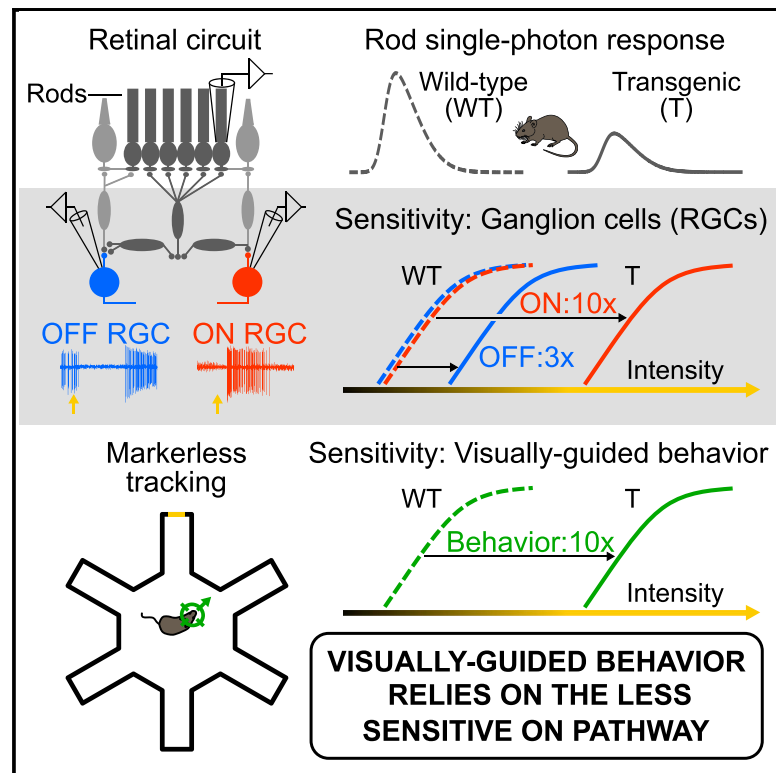# Paradoxical Rules of Spike Train Decoding Revealed at the Sensitivity Limit of Vision

Lina Smeds,[1,3] Daisuke Takeshita,[1,3] Tuomas Turunen,[2] Jussi Tiihonen,[1,2] Johan Westö,[2] Nataliia Martyniuk,[2] Aarni Seppänen,[2] and Petri Ala-Laurila[1,2,4,*]

[1]Faculty of Biological and Environmental Sciences, Molecular and Integrative Biosciences Research Programme, University of Helsinki, 00790 Helsinki, Finland
[2]Department of Neuroscience and Biomedical Engineering, Aalto University, 02150 Espoo, Finland
[3]These authors contributed equally
[4]Lead Contact
*Correspondence: petri.ala-laurila@helsinki.fi
https://doi.org/10.1016/j.neuron.2019.08.005

SUMMARY

All sensory information is encoded in neural spike trains. It is unknown how the brain utilizes this neural code to drive behavior. Here, we unravel the decoding rules of the brain at the most elementary level by linking behavioral decisions to retinal output signals in a single-photon detection task. A transgenic mouse line allowed us to separate the two primary retinal outputs, ON and OFF pathways, carrying information about photon absorptions as increases and decreases in spiking, respectively. We measured the sensitivity limit of rods and the most sensitive ON and OFF ganglion cells and correlated these results with visually guided behavior using markerless head and eye tracking. We show that behavior relies only on the ON pathway even when the OFF pathway would allow higher sensitivity. Paradoxically, behavior does not rely on the spike code with maximal information but instead relies on a decoding strategy based on increases in spiking.
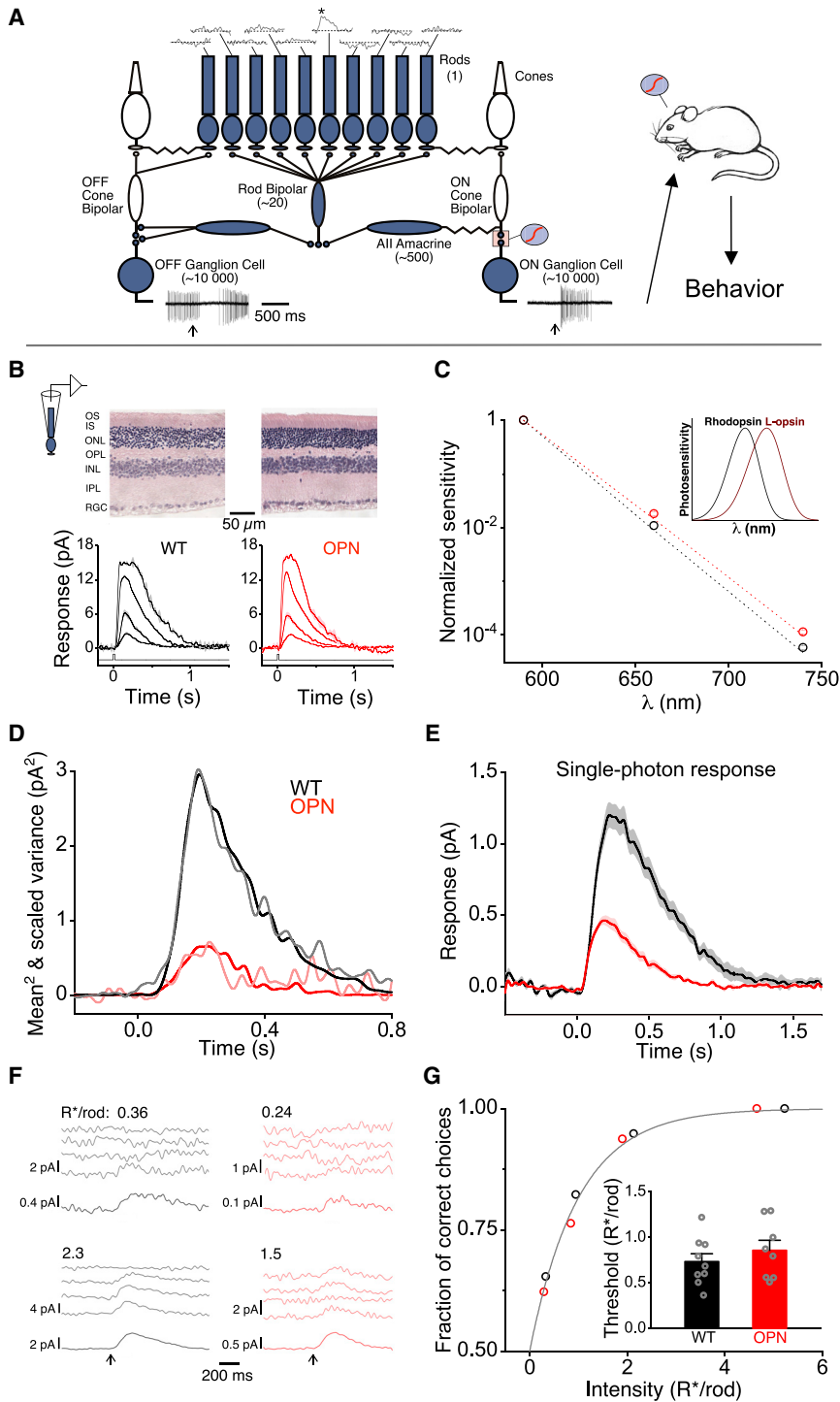
INTRODUCTION

It has been difficult to link animal behavior to its underlying neural spike trains due to the complexity of neural circuits and animal behavior. In the absence of a quantitative link between spike-resolution neural data and behavior, it has been hypothesized that behavior should rely on the neural codes providing the highest information content relevant for a particular behavior (reviewed in Nirenberg, 2012). Vision at its sensitivity limit offers a unique framework to test this idea, since the visual sensitivity of dark-adapted humans and mice approaches the limits set by the quantal nature of light (Hecht et al., 1942; Naarendorp et al., 2010). Furthermore, previous work on amphibians has demonstrated a correlation between the sensitivity threshold of the most sensitive retinal output neurons, retinal ganglion cells (RGCs), and visually guided behavior at the lowest light levels (Aho et al., 1988, 1993a, 1993b). Both the number of feasible neu-

ral computations and the types of RGCs that can contribute to vision are limited due to the sparseness of photons at the visual threshold. Seeing is then based on single-photon responses originating in a small number of rods and traversing the mammalian retina via the rod bipolar pathway (Figure 1A; reviewed in Field et al., 2005). These sparse signals utilize the same retinal circuitry (rod bipolar circuitry) until the last synapse before the RGCs and only there diverge into two different information streams, ON and OFF pathways. The ON pathway reports single-photon signals by increases in firing, whereas the OFF pathway reports single-photon signals by decreases in firing. The last synapse of the ON pathway, but not that of the OFF pathway, involves a thresholding nonlinearity eliminating most neural noise at the cost of losing a significant proportion of single-photon responses (Ala-Laurila and Rieke, 2014). This nonlinearity makes the ON and OFF RGC outputs asymmetric in their tradeoff between sensitivity and reliability (reviewed in Takeshita et al., 2017). The ON pathway provides the brain with a thresholded, low-noise readout of single-photon signals coded by increases in spiking; the OFF pathway provides a slightly more sensitive but noisier readout coded by decreases in spiking. It is unknown how behavior depends on these two distinctly different readouts of sparse signals originating from single photons in the retinal input.

Previous studies at the level of the lateral geniculate nucleus (LGN) neurons and visually guided saccadic reaction times in monkeys have provided valuable information about the differing functional roles of the ON and OFF pathways by showing that pharmacological blockage of the ON pathway compromises detection of light increments, but not that of light decrements, at cone-driven light levels (Schiller, 1982; Schiller et al., 1986; Dolan and Schiller, 1989; reviewed in Schiller, 1992, 2010). Furthermore, theoretical arguments suggest that the split of visual information into parallel ON and OFF pathways allows more efficient coding of visual scenes compared to, for example, an ON-ON system within a limited spike budget (Gjorgjieva et al., 2014). However, rigorous linking of the neural spike trains from particular RGC types to precisely quantifiable visually guided behavior has been missing. This linking would be particularly hard at cone-driven light levels, where retinal circuits carry out a rich set of computations impacting the spike output of ~40 distinct RGC types in the mouse retina (Baden et al., 2016; Bae et al., 2018; Rheaume et al., 2018).

A

Rods
(1)

Cones

OFF Cone Bipolar

Rod Bipolar (~20)

ON Cone Bipolar

OFF Ganglion Cell (~10 000)

AII Amacrine (~500)

ON Ganglion Cell (~10 000)

500 ms

Behavior

B

OS
IS
ONL
OPL
INL
IPL
RGC

50 μm

WT

OPN

Response (pA)

Time (s)

C

Normalized sensitivity

Rhodopsin L-opsin

Photosensitivity

λ (nm)

λ (nm)

D

Mean² & scaled variance (pA²)

WT
OPN

Time (s)

E

Single-photon response

Response (pA)

Time (s)

F

R*/rod: 0.36

0.24

2 pA

1 pA

0.4 pA

0.1 pA

2.3

1.5

4 pA

2 pA

2 pA

0.5 pA

200 ms

G

Fraction of correct choices

Threshold (R*/rod)

WT OPN

Intensity (R*/rod)

Figure 1. The Rod Bipolar Pathway and a Comparison of OPN and WT Rod Response Properties

(A) The rod bipolar pathway of the mammalian retina mediating single-photon signals originating in rods at the visual threshold. Only a few rods among a thousand or so contain signals (denoted by *), whereas the rest generate noise. The convergence of rod signals is shown at different levels of the circuit (Dunn and Rieke, 2008). The last synapse of the ON (but not the OFF) pathway operates as a thresholding nonlinearity (Ala-Laurila and Rieke, 2014). This nonlinearity segregates pooled signals from pooled neural noise. The retinal output neurons, ON and OFF ganglion cells, send the signals to the brain. The behavioral performance of the animal in a visual test provides the final output for visual performance.

(B–G) Comparison of the response properties and sensitivities of OPN and WT mouse rods.

(B) Paraffin sections of a 6- to 7-month-old WT (top left) and OPN retina (top right) stained with H&E and showing normal retinal morphology: OS, photoreceptor outer segments; IS, photoreceptor inner segments; ONL, outer nuclear layer; OPL, outer plexiform layer; INL, inner nuclear layer; IPL, inner plexiform layer; RGC, retinal ganglion cell layer. Responses from one WT rod (bottom left, black; mean ± SEM) and one OPN rod (bottom right, red) to a sequence of flashes (20 ms, given at $t = 0$) of increasing intensities (R*/rod/flash). WT: 2.9 (n = 20 flashes), 8.1 (n = 10), 30 (n = 10), and 98 (n = 2); OPN (R*/rod/flash): 3.4 (n = 50), 12 (n = 10), 38 (n = 10), and 144 (n = 2). Half-saturating intensities (I_s; R* / rod) and maximum dark currents (R_{max}; pA) for these example cells were $I_s = 11.9$ R* / rod, $R_{max} = 16.4$ pA (WT); $I_s = 23.8$ R* / rod; $R_{max} = 19.7$ pA (OPN). For the population data (I_s, R_{max}) = 14.2 ± 1.4 R* / rod, 16.4 ± 0.8 pA (WT, n = 32 rods); 31.1 ± 2.7 R* / rod, 13.2 ± 0.8 pA (OPN, n = 40 rods).

(C) Normalized spectral sensitivities (mean ± SEM) of WT (black, n = 8) and OPN (red, n = 16) mouse rods as measured using light-emitting diodes (LEDs) with peak sensitivities at three different wavelengths. The percentage of L-cone pigment in OPN rods is estimated by fitting linear combinations of spectral templates (Govardovskii et al., 2000) for rhodopsin ($\lambda_{max} = 497$ nm) and human L-cone pigment ($\lambda_{max} = 557$ nm). WT rods were fit well by a template containing 0% L-cone pigment (black dashed line), and OPN rods were fit best by a template containing 0.37% of L-cone pigment. Inset: spectral templates (Govardovskii et al., 2000) for mouse rhodopsin and human L-cone pigment.

(D) Examples of variance analysis for one WT and OPN rod to estimate the size of single-photon response. The square of the mean response (WT, black; OPN, red) and scaled time-dependent ensemble variance (WT, gray; OPN, pink) of dim flash responses in one WT and one OPN example cell (WT, 80 flashes; OPN, 29 flashes). The scaling factor of variance provides an estimate of the mean number of photoisomerizations produced by the flash: 1.1 R* (WT); 2.3 R* (OPN).

(E) Single-photon responses (mean ± SEM) for the population of WT (black, n = 20) and OPN (red, n = 24) rods. Amplitudes: 1.26 ± 0.11 pA (WT) and 0.45 ± 0.04 pA (OPN).

(F) Two-alternative forced choice (2AFC) procedure to characterize rod sensitivity as shown for one WT and one OPN rod; responses to dim flashes produced on average 0.36 and 2.3 R* (WT, left) and 0.24 and 1.5 R* (OPN, right). Four example traces are shown at each light intensity and the average response calculated across 80–180 trials are shown at the bottom in each case.

Our aim here is to utilize the ON and OFF pathways as a quantitative tool to attack our central question: does animal behavior rely on the spike code that provides the highest information content for a particular visual computation—in this case, light detection? We report experiments where we, for the first time, directly link the behavioral performance of mice with that of RGCs at the sensitivity limit of vision in a quantitative manner. To do so, we relied on two key factors. First, we used a transgenic mouse line with decreased single-photon response amplitude to differentiate the sensitivities of the most sensitive ON and OFF RGC types at the sensitivity limit of vision, while otherwise causing minimal changes in retinal signaling. Second, we estimated the sparse photon distributions originating from visual stimuli and arriving on the retinas of freely swimming mice in behavioral experiments using novel markerless tracking of the mouse body, head, and eye movements. Finally, we correlated the most sensitive ON and OFF RGC population codes with the behavioral performance, using ideal observer models tightly constrained by the RGC measurements and the retinal stimulus trajectories derived from the tracked behavioral experiments. Surprisingly, we find that behavior relies only on the ON pathway, even when the OFF pathway would allow higher sensitivity. Our results show that behavior does not utilize the maximal information in the spike trains across the ON and OFF pathways but uses a decoding strategy based only on increases in spiking in the ON pathway.

RESULTS

OPN Mouse Rods Have 3-Fold Smaller Single-Photon Responses than WT Mouse Rods

We recorded the responses of dark-adapted rods from wild-type (WT) mice and a transgenic mouse strain (OPN1LW [Fu et al., 2008], hereinafter denoted as OPN). The latter strain was originally developed for studying rod noise, since it has an elevated rate of spontaneous pigment activations due to co-expression of a low level of human L-cone pigment with rhodopsin in its rods. Retinal morphology and general rod response properties showed no significant differences (Figure 1B), despite the presence of 0.4% human L-cone pigment in OPN rods (Figure 1C). This proportion is estimated to increase the rate of spontaneous pigment activations 5-fold compared to WT (Fu et al., 2008). Importantly, however, OPN rods had 2.8-fold smaller single-photon responses than WT rods (Figures 1D and 1E), which was also evident in the intensity-response relations: the flash intensity (in R*/rod) needed to elicit a half-saturated response was on average 2.2-fold higher for OPN rods than for WT rods in the population data (example rods are shown in Figure 1B). We used an ideal observer model to explore whether there were any differences in the detectability of single-photon responses in rods between the two strains (STAR Methods). Figures 1F and 1G show that the detectability of weak flashes in both WT and OPN rods was limited only by the theoretical limit set by the Poisson distri-

bution of photon arrivals (gray line in Figure 1G). This analysis demonstrates that OPN rods with a lower signal-to-noise ratio due to smaller single-photon amplitude and increased pigment noise can still function as single-photon detectors. In summary, the OPN mouse retina provides a specific experimental tool at the visual threshold with significantly smaller single-photon amplitude but still with a sufficient signal-to-noise ratio for the detectability of single-photon responses in rods.

The Smaller Single-Photon Responses in OPN Rods Break the Sensitivity Symmetry between the Most Sensitive ON and OFF RGC Types

We hypothesized that the smaller single-photon response amplitude in the OPN rods would cause a larger proportion of single-photon responses to be lost in the thresholding nonlinearity unique to the ON pathway and hence break the sensitivity symmetry between the most sensitive ON and OFF RGC types (Figure 1A; see also Ala-Laurila and Rieke, 2014). To test this, we recorded the spike outputs of ON and OFF sustained alpha ganglion cells (hereinafter simply referred to as ON-S and OFF-S RGCs) in OPN and WT mice at their sensitivity limit. Alpha ganglion cells are easy to target due to their large somas, and they are also the closest homologs among the mouse RGC types to the parasol RGCs in the primate retina (reviewed in Sanes and Masland, 2015), where the nonlinearity specific to the ON pathway in darkness was originally found (Ala-Laurila and Rieke, 2014). More importantly, alpha RGCs are also considered the primary candidates for mediating light detection at the visual threshold due to their high sensitivity (reviewed in Takeshita et al., 2017). To validate that ON-S and OFF-S RGCs indeed belong to the most sensitive RGC types in the mouse retina, we targeted all RGCs adjacent to ON-S and OFF-S RGCs in the RGC mosaic (Figure 2A). Figure 2B shows spike traces and normalized average post-stimulus-time histograms (PSTHs) of the 21 RGCs shown in Figure 2A (including one ON-S and one OFF-S RGC) that responded to flashes in the intensity range tested. These responses are positioned along the intensity axis at the intensity where each RGC responded in >80% of the trials. ON-S and OFF-S RGCs responded to light intensities that were ~7- to 700-fold dimmer than the intensities needed to elicit responses in the remaining 19 unidentified cells in this sample (14 of the cells shown in Figure 2A did not respond to the stimulus at all at these light intensities). The key question is how many RGCs need to be recorded from across different preparations to ensure that measurements have been taken from all or close-to-all different RGC types in the mouse retina. We used previous density estimates of different RGC types in the mouse retina (Baden et al., 2016) to assess the probability of measuring from at least one RGC of each type as a function of the total number of cells (N) tested across different independent preparations (Figure 2C). The total number of "other" RGCs tested in our experiments in both WT and OPN retinas was ~200 giving a high probability

---

(G) Probability of correct choice as obtained in 2AFC procedure for the same example cells as shown in (F). The continuous line shows a theoretical limit for optimal performance in single-photon detection arising from Poisson distribution: P(correct choice) = $1 - (e^{-I}/2)$, where I = mean intensity in R*. Inset: collected data on the rod threshold determined as the intensity (R*) corresponding to 75% probability of response (mean ± SEM) for WT (0.73 ± 0.09; n = 9 rods) and OPN (0.86 ± 0.01; n = 8). The thresholds did not differ significantly between WT and OPN rods (p = 0.39, unpaired Student's t test).
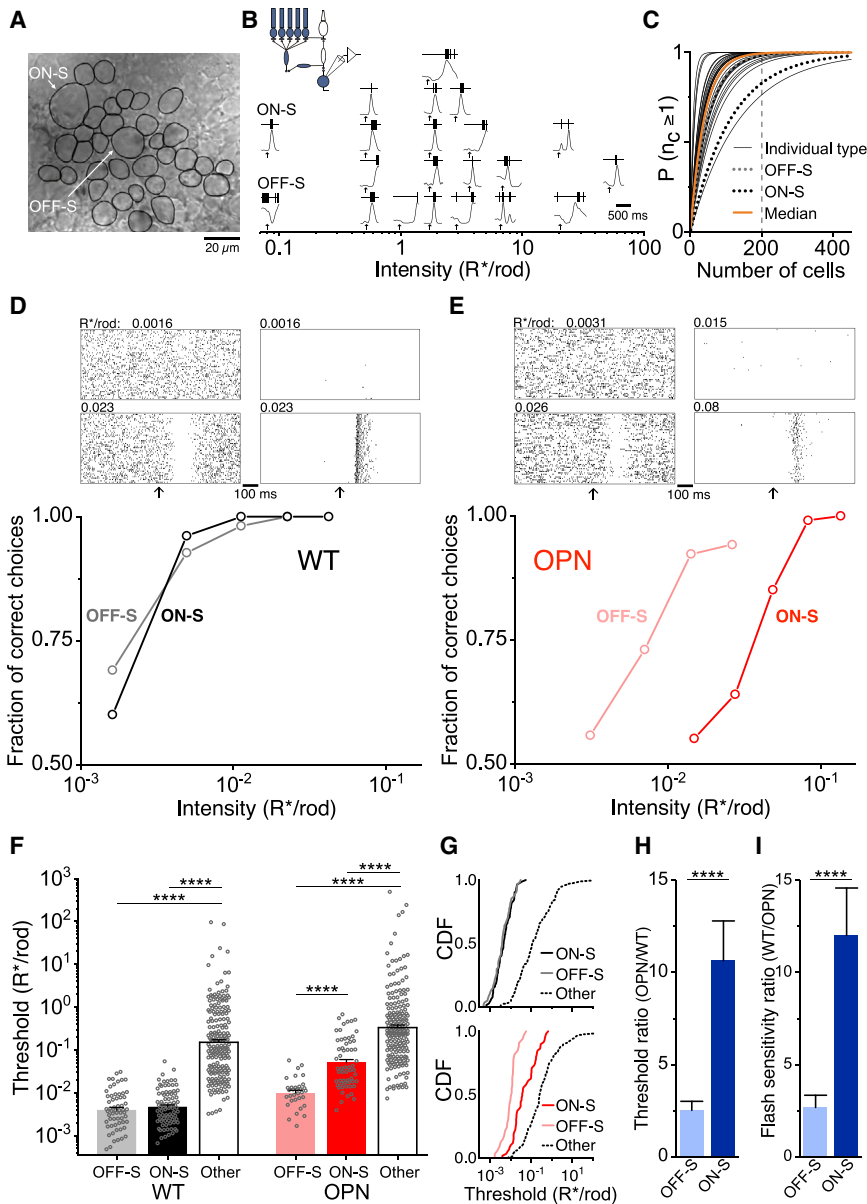
Figure 2. Comparison of RGC Sensitivities in WT and OPN Mice

(A) Bright-field image of RGCs in a flat-mounted piece of WT mouse retina with targeted RGC somas highlighted.

(B) Spike responses and normalized average post-stimulus time histograms (PSTHs) (n = 100–300 responses) to flashes (20 ms) shown at the intensity corresponding to response probability of >80%. Data are shown for the 21 out of 35 RGCs tested in (A) that responded to the tested stimuli. The remaining RGCs did not respond to the highest intensity tested (100 R*/rod/flash in this mount).

(C) The probability of finding at least one RGC of a specific type ($n_c \geq 1$; RGC densities from Baden et al., 2016) as a function of the total number of RGCs sampled across retinal mosaics as in (A) (STAR Methods). The dashed line indicates the total number of 200 cells, which is close to the number probed both in WT and OPN mouse strains (WT, 193 cells; OPN, 194 cells). The probabilities are lower-limit estimates, since those cells that did not respond within the intensity range tested (79 cells in WT and 77 in OPN) were not included in this number. These cells were either not sensitive enough and/or some of them could have been displaced amacrine cells.

(D) WT ON-S RGC (top right) and OFF-S RGC (top left) responses to dim flashes delivered at the time of the arrow. Each raster shows 50 trials in response to flashes of a constant intensity indicated in the top left corners (in R*/rod). A two-alternative forced choice (2AFC) procedure to characterize RGC sensitivity (fraction of correct choices) shown for the same WT ON-S (black) and the OFF-S (gray) RGC (bottom). The light intensity yielding 75% correct choices was defined as the RGC threshold.

(E) The same as (D) but for OPN ON-S (red) and OFF-S (pink) RGCs. Note that a significantly higher flash intensity is used for OPN ON-S RGCs than for WT ON-S RGCs.

(F) Collected data on RGC thresholds (mean ± SEM) for WT RGCs (OFF-S, 0.0040 ± 0.0006 R*/rod, n = 61 cells; ON-S, 0.0047 ± 0.0005, n = 82; other RGC types, 0.15 ± 0.02, n = 193) and OPN RGCs (OFF-S, 0.010 ± 0.001, n = 33; ON-S, 0.050 ± 0.009, n = 59; other, 0.33 ± 0.05, n = 194). ON-S and OFF-S alpha RGCs are significantly more sensitive than other RGC types both in WT and OPN strains, and OPN ON-S RGCs are significantly less sensitive than OPN OFF-S RGCs (pairwise comparisons are indicated by horizontal lines; ****p < 10^{-4}, unpaired Welch's t test).

(G) Cumulative distribution functions for the RGC threshold data in (F) for WT (top) and OPN (bottom) RGCs.

(H) The ratio of thresholds (OPN/WT) for ON-S and OFF-S RGCs were 10.6 and 2.5, respectively (significantly different: p < 10^{-6}, unpaired Welch's t test; STAR Methods).

(I) The ratios of flash sensitivities (= response per photoisomerization) for ON-S and OFF-S RGCs were 12.0 and 2.7, respectively (significantly different [p < 10^{-5}, unpaired Welch's t test]). The agreement between the threshold ratios and the sensitivity ratios indicates that the former are not significantly affected by changes in noise but instead by changes in the size of the visual signals originating from single-photon responses propagating the retina. For OFF-S cells, but not for ON-S cells, the flash sensitivity difference can already be mostly explained by the 3-fold smaller single-photon response amplitude in OPN rods. Note that the ratio of OPN to WT is calculated in (H), while the ratio of WT to OPN is used in (I), since threshold and sensitivity are inversely related.

Error bars represent SEMs.

of finding each individual RGC type (Figure 2C, dashed line) and 90% joint probability (STAR Methods) that we probed all or missed maximally only one of the previously identified RGC types (Baden et al., 2016).

For a more rigorous analysis of RGC sensitivities, we characterized the detectability of responses across all RGCs to dim flashes similarly as we did for rods, with an ideal observer model considering both the light responses and the tonic firing
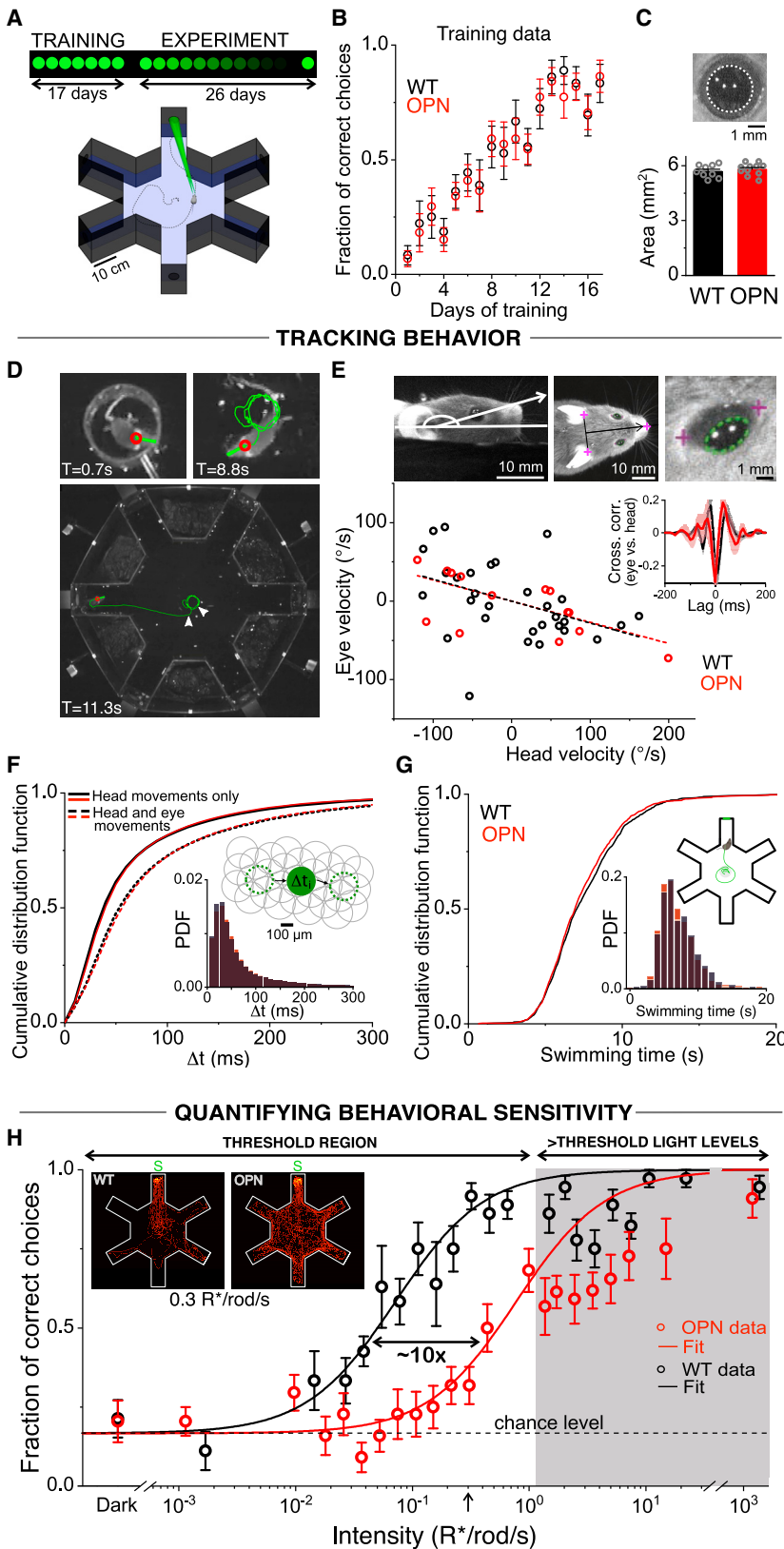
Figure 3. Comparison of Visually Guided Behavioral Performance in a Dim-Light Detection Task for WT and OPN Mice

(A) A schematic picture of the 6-arm water maze used to measure the behavioral sensitivity (below). The tracked swimming route of one mouse is shown as a dotted line; the stimulus light reaching the eye is shown in green. The protocol (top) consisted of a training period with a constant bright stimulus light that was followed by an experimental period where the light intensity was made dimmer in each testing day.

(B) WT and OPN mice both reached >80% correct-choice performance in the 17-day training period showing no difference in learning the task (p > 0.3, unpaired Student's t test). Each data point represents the mean over four trials for every mouse (n = 11 OPN mice; n = 9 WT mice), and a correct choice was defined based on the first corridor entered during each trial.

(C) The pupil areas as measured in experimental conditions were similar for both strains (p = 0.47, unpaired Student's t test): 5.70 ± 0.11 mm^2 (n = 9 mice, WT) and 5.81 ± 0.10 mm^2 (n = 11 mice, OPN).

(D) Head direction and mouse position as tracked during one swimming trial using our automatic markerless video tracker (bottom; white arrows indicate the mouse position corresponding to the top panels). Initialization of a swimming trial in a transparent tube (top left panel). Tracking data right after the mouse has been released from the tube (top right). Red circle, tracked point of the mouse head; thick green line, head direction; T, time since trial onset.

(E) The effects of compensatory eye movements (vestibulo-ocular reflex) were estimated in separate trials. The water surface constrains head movements to the axis perpendicular to it (yaw axis) while also causing the mice to keep their heads in upward tilted position (top left) and allowing simultaneous markerless head and eye tracking from above (top right: tracked landmarks in pink and pupil outlined in green; pilocarpine eye drops were used to contract the pupils; see STAR Methods). The bottom panel shows a negative correlation between the angular velocities of head and eye movements, in line with compensatory eye movements (slope or gain indicated by fitted dashed lines). The strength of the compensatory eye movements, quantified by a gain value, were similar for both strains: WT: -0.28 ± 0.11; OPN: -0.27 ± 0.086 (p = 0.95, F-test). The inset shows the cross correlation between eye and head movements.

(F) Estimation of the duration of time (Δt) that the stimulus stayed within the receptive field of a single RGC for WT and OPN mice. The position and direction of the mouse head was captured by the tracker (D), and the stimulus projection onto the grid of retinal ganglion cells was computed (see STAR Methods and Figure S2 for details) to obtain the probability density function of Δt for WT (black, n = 887 swimming trials) and OPN (red, n = 1,079 swimming trials) mice (inset). The main panel shows the cumulative distribution function of Δt (CDF) for WT and OPN assuming no compensatory eye movements (solid lines) and compensatory eye movements (dashed lines). Median Δt: 38 ms (WT, with head movements only, solid line), 39 ms (OPN, solid line), 53 ms (WT, with head and eye movements, dashed line), and 56 ms (OPN, dashed line).

(legend continued on next page)

rates of the RGCs (STAR Methods). Figures 2D and 2E exemplify the spike rasters of OFF-S and ON-S RGCs in response to different light intensities in WT and in OPN retinas. OFF-S cells had a high tonic firing rate in both WT (50 ± 2 Hz, n = 61 cells, mean ± SEM) and OPN (62 ± 3 Hz, n = 33 cells) and responded to dim flashes by gaps in their tonic firing, whereas ON-S cells had a low tonic firing rate and responded to flashes by increasing their firing rates, similar to primate OFF and ON parasol RGCs (Ala-Laurila and Rieke, 2014). The difference between thresholds (defined as 75% correct choices in a two-alternative forced choice task) of ON-S and OFF-S RGCs in WT mice was small and not statistically significant (Figure 2F; p = 0.3, unpaired Student's t test), consistent with an earlier study on primate ON and OFF parasol cells (Ala-Laurila and Rieke, 2014). Furthermore, ON-S RGCs and OFF-S RGCs were on average >30-fold more sensitive than the average "other" RGC type (Figures 2F and 2G), suggesting that ON-S and OFF-S alpha RGCs are indeed good representatives of the most sensitive RGC types in the mouse retina. A few other RGCs in the pool of "other cells" came close to the sensitivities of ON-S and OFF-S RGCs. Three out of the four most sensitive other RGCs could be identified as OFF transient alpha RGCs, consistent with previous findings suggesting that OFF sustained and OFF transient alpha RGCs have similar sensitivity thresholds (Murphy and Rieke, 2011). More importantly, no other RGC was more sensitive than the most sensitive ON-S and OFF-S RGCs in WT mice. It should also be noted that our primary findings are in fact insensitive to the existence of such other RGC types that come close to ON-S and OFF-S RGCs in sensitivity (see Discussion).

In contrast to the sensitivity symmetry found between WT OFF-S and ON-S RGCs, there was a prominent ON-OFF asymmetry in OPN mice. The thresholds of ON-S RGCs were 5-fold higher than those of OFF-S RGCs on average (Figures 2E and 2F). However, OPN OFF-S and ON-S RGCs were both still on average more sensitive than the average other OPN RGC type (Figure 2F). Most importantly, comparing the two mouse strains, the OPN-WT threshold ratio was 10.6-fold for ON-S RGCs and only 2.5-fold for OFF-S RGCs (Figure 2H). This asymmetry is consistent with the hypothesis that the thresholding nonlinearity in the ON pathway caused a more significant loss of the smaller single-photon events in OPN compared to WT mice. The threshold differences between WT and OPN can be wholly explained by the differences in flash sensitivity (response size per R*) for both ON-S and OFF-S cells (Figure 2I), suggesting that possible noise differences due to an elevated rate of spontaneous pigment activations in OPN rods have a negligible effect on the RGC thresholds.

The Behavioral Light Detection Limit of OPN Mice Is Shifted ~10-Fold to Higher Intensities Compared to WT Mice, in Line with the Shift of ON-S RGC Sensitivities

Now that we had established a sensitivity asymmetry between the most sensitive ON and OFF RGCs in OPN mice, we could use this strain to address our primary question: does the behavioral threshold depend on the most sensitive retinal output signals (i.e., those of OFF-S RGCs)? First, we established a behavioral paradigm allowing us to link RGC sensitivities with visually guided behavior at the sensitivity limit (Figure 3A). Second, we compared other key factors besides RGC sensitivities between WT and OPN mice that could impact behavioral sensitivity, including learning performance in the behavioral task (Figure 3B), pupil sizes (Figure 3C), and behavioral strategy relying on markerless tracking of mouse head direction, location, and eye movements (Figures 3D–3G; Videos S1 and S2). We quantified the behavioral sensitivity by measuring the probability of finding the stimulus channel in a water maze as a function of light intensity (Figure 3H), which was our primary sensitivity metric.

The mice were initially trained to associate an escape ramp from the water with a bright light stimulus until both mouse strains were able to locate the stimulus channel with similar accuracy (>80%, reached after 17 days of training; Figure 3B; no differences between WT and OPN mice, p > 0.3, unpaired Student's t test). Training was followed by the experiment in which the probability of finding the stimulus channel was measured across light intensities (Figure 3A, top; STAR Methods) until the stimulus light was so dim that the mice could no longer locate the stimulus (meaning that the fraction of correct choices was 1/6 = chance level; dashed line in Figure 3H). The pupil areas of WT and OPN mice did not differ in the experimental conditions (Figure 3C; p = 0.47, unpaired Student's t test). Similarly, we observed no differences in the sampling strategy of visual cues in the water maze between the two mouse strains, as assessed by tracking the body and head positions during the task and estimating the distribution of durations that the stimulus spot would spend within the receptive field of alpha RGCs in a retinal mosaic (Figures 3D, 3F, and S2; STAR Methods). Furthermore, within measurement accuracy, OPN and WT mice showed similar amounts of stabilizing or compensatory eye movements (vestibulo-ocular reflex [VOR]; Figure 3E; dashed line in Figure 3F), which is roughly in line with previous results on freely moving mice (Payne and Raymond, 2017; Meyer et al., 2018). The distributions of swimming times required to reach the first channel chosen in the experiment were also similar for WT and OPN mice (Figure 3G; no difference, p = 0.38, Kolmogorov-Smirnov test). In summary, no differences in learning the task, eye optics, or behavioral strategy between WT and OPN mice were found.

(G) Swimming times of mice from the beginning of the trial until entering the first corridor. Median swimming times were 6.9 s (OPN) and 7.0 s (WT). The inset shows the probability density function of swimming times over all intensities for OPN (red, n = 992 swimming trials) and WT (black, n = 813) mice. The main figure shows the cumulative distribution functions.

(H) Behavioral performance for WT (n = 9) and OPN (n = 11) mice in a dim-light detection task. Fitted functions are modified Hill functions (STAR Methods) showing an 11-fold shift in sensitivity between WT and OPN mice. The fits were applied in the low-intensity region (<1 R*/rod/s), where performance improved monotonically with increasing light intensity (threshold region). The insets show the tracked population swimming trajectories (four swimming trials per mouse) for the stimulus intensity where the greatest difference in behavioral performance was seen (0.3 R*/rod/s, indicated with an arrow in the main panel). The correct corridor, the stimulus corridor, is marked with an S.

All error bars represent SEMs. See also Figures S1–S4.

Now that we had excluded other key factors unrelated to RGC sensitivity that could cause differences in behavioral sensitivity between WT and OPN mice, we focused on measuring the behavioral sensitivity limit. A significant difference in performance between OPN and WT mice was immediately evident in the probability of finding the stimulus channel in the water maze task. The inset in Figure 3H illustrates this difference in swimming trajectories recorded for the two mouse populations at a single dim light intensity (0.3 R*/rod/s) with the stimulus channel plotted on top; WT mice swam almost exclusively toward the stimulus channel at this stimulus intensity, whereas OPN mice often needed to explore multiple channels in the maze before finding the stimulus. The main panel of Figure 3H shows the frequency of finding the light stimulus as a function of light intensity for both OPN and WT mice. Both strains showed a monotonic rise in the fraction of correct choices as a function of light intensity from darkness to ∼1R*/rod/s stimulus intensity (entitled "threshold region" in Figure 3H), after which performance showed no steady improvement with increasing light levels ("> threshold light levels," gray shading in Figure 3H). We focused our analysis on the threshold region, since it is the most relevant intensity range when we are concerned with absolute visual sensitivity and its relation to RGC signaling. In this region, there was an 11.0-fold shift in the psychometric function toward higher light intensities for the OPN mice as compared with the WT mice, matching the OPN-WT sensitivity shift of ON-S RGCs (10.6-fold), but not that of OFF-S RGCs (2.5-fold).
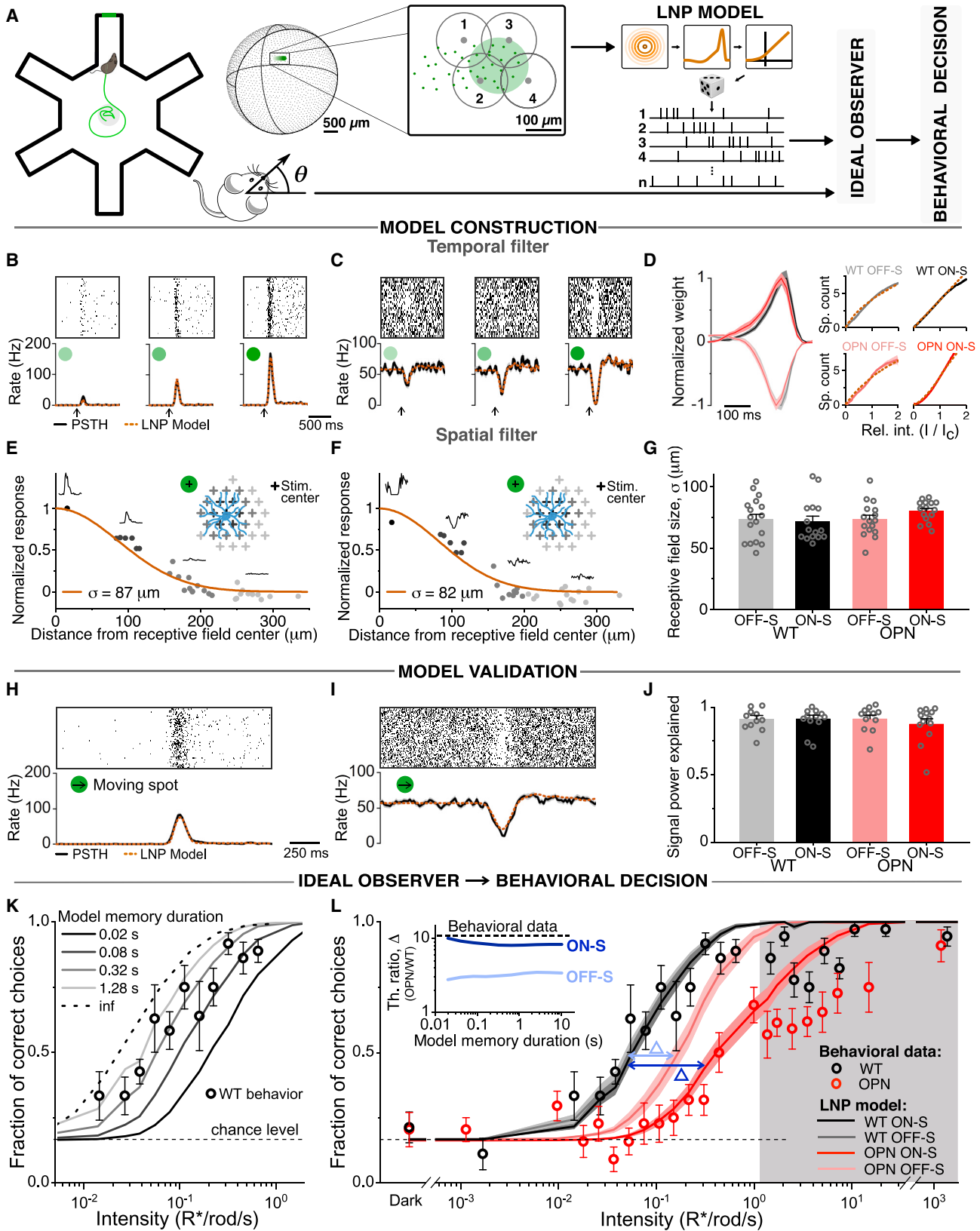
The Behavioral Threshold Relies on Information from Retinal ON-S RGCs Only

The close agreement between the OPN and WT sensitivity differences as measured in ON-S RGCs and behavior suggests that behavior relies on ON-S. By contrast, if behavior relied on OFF-S RGCs, the difference in behavioral sensitivity would be much smaller. However, this comparison is complicated by the fact that the stimuli experienced by the RGCs are not identical in our single-cell RGC recordings and in the behavioral experiments. In the former, RGC thresholds are obtained by using flash stimuli, whereas in the latter, the RGCs experience a continuously moving stimulus spot consisting of a sparse rain of photons on the retinas of freely swimming mice (Figure 4A). Furthermore, the mouse brain has access to the spike trains provided by the populations of RGCs of distinct types until the decision is made. To predict the ultimate limits of behavioral performance, we constructed four different ideal observer models, one for ON-S RGCs and one for OFF-S RGCs for both the WT and the OPN mouse strains (Figure 4A). These ideal observers were assumed to have access to the information from the full cell mosaic of a particular RGC type, as well as the information on the head direction of the mouse, allowing linking of the RGC spike codes to the visual world. Furthermore, the ideal observers had a "memory" component across time integrating evidence from the RGCs belonging to the retinal trajectory of the tracked route of the stimulus projection. First, we estimated the movement of the sparse stimulus on the retina based on the tracked swimming trajectories and eye optics of the same mice that were used for the behavioral tests. We took into account the impact of stabilizing eye movements (Figures 3E and 3F; see

also Figure S8C for model robustness related to compensatory eye movements). Second, we constructed a model for mapping sparse photon hits on the retinal surface into RGC responses using a time-space separable linear-nonlinear Poisson (LNP) model with a fixed output nonlinearity (STAR Methods; Figures 4B–4J). Third, we constructed an ideal observer model that selected the most likely stimulus location based on the RGC responses across the entire swimming trajectory of the mouse (STAR Methods; Figure S7).

To construct LNP models for WT and OPN ON-S and OFF-S RGCs, we fitted temporal filters to the RGC responses to brief light flashes of various intensities, as exemplified for an OPN ON-S (Figure 4B) and for an OFF-S RGC (Figure 4C). The filters were monophasic showing that ON-S and OFF-S RGCs responded by increasing or decreasing their firing rates, respectively (Figure 4D, left panel), and the estimated intensity-response functions matched population data in the relevant low-intensity range (Figure 4D, right panel). The spatial filters were obtained by fitting a two-dimensional (2D) Gaussian to the responses elicited by dim spots presented in different locations of the receptive field, as shown for an OPN ON-S RGC (Figure 4E) and OPN OFF-S RGC (Figure 4F). There were no significant differences in the size of receptive fields across the four RGC types studied here at their sensitivity threshold (Figure 4G). For validation, LNP model predictions were compared with actual RGC responses to dim stimulus spots moving on the retinas with the median speed derived from the automated mouse tracking data (Figure 4H, ON-S; Figure 4I, OFF-S). The model predicted the responses of RGCs to these sparse stimuli accurately both in WT and OPN mice (Figure 4J), in line with the notion that ON-S and OFF-S RGCs simply sum photons in time and space in their receptive fields without more complex motion computations at these extremely low light levels (Figure S5). This is consistent with previous findings that retinal circuit mechanisms favoring more complex computations (such as motion-sensitivity and high-resolution spatial subunits) are sacrificed for sensitivity at low light levels (Kuo et al., 2016; Grimes et al., 2014; Yao and Field, 2019).

Now that we had established a model allowing us to predict the responses of the entire mosaic of a particular RGC type to a stimulus projection across the entire swimming trajectory of a mouse, we wanted to assess how closely behavior matches the optimal readout of ON-S and OFF-S RGC-mosaic spike trains. We used an ideal observer model that had access to the responses of a full RGC mosaic (ON-S or OFF-S RGCs in either WT or OPN mice) and made a decision about the most likely stimulus location by comparing the total spike count from all possible locations across time (STAR Methods). The best performance is obtained by an ideal observer with a perfect memory, having access to all RGC spikes across the entire swimming trajectory of the mouse. The behavioral data for WT mice fall remarkably close (within ∼3-fold) to this ultimate limit (noiseless readout of population spikes and a perfect memory across the entire swimming trajectory; Figure 4K, dashed line). By restricting the memory component, less "ideal" versions of the ideal observer can be created. The other curves in Figure 4K (solid lines) represent model fits with different (shorter) memory durations (square-window access to the spikes of the RGC

A

LNP MODEL

IDEAL OBSERVER

BEHAVIORAL DECISION

500 μm

100 μm

θ

1
2
3
4
n

MODEL CONSTRUCTION
Temporal filter

B

Rate (Hz)

200

PSTH   LNP Model   500 ms

C

Rate (Hz)

100

50

0

Spatial filter

D

Normalized weight

1

0

-1

WT OFF-S   WT ON-S

OPN OFF-S   OPN ON-S

100 ms

Sp. count

5

0

Rel. int. (I / I_C)

E

Normalized response

1

0.5

0

σ = 87 μm

+Stim. center

Distance from receptive field center (μm)

F

Normalized response

1

0.5

0

σ = 82 μm

+Stim. center

Distance from receptive field center (μm)

G

Receptive field size, σ (μm)

100

50

0

OFF-S ON-S   OFF-S ON-S
   WT   OPN

MODEL VALIDATION

H

Rate (Hz)

200

100

0

Moving spot

PSTH   LNP Model   250 ms

I

Rate (Hz)

100

50

0

J

Signal power explained

1

0.5

0

OFF-S ON-S   OFF-S ON-S
   WT   OPN

IDEAL OBSERVER → BEHAVIORAL DECISION

K

Fraction of correct choices

1.0

0.5

0.0

Model memory duration
0.02 s
0.08 s
0.32 s
1.28 s
inf

WT behavior

chance level

Intensity (R*/rod/s)

L

Fraction of correct choices

1.0

0.5

0.0

Th. ratio, Δ (OPN/WT)

10

1

Behavioral data

ON-S

OFF-S

0.01 0.1   1   10
Model memory duration (s)

Dark   10⁻³   10⁻²   10⁻¹   1   10   10³

Intensity (R*/rod/s)

Behavioral data:
○ WT
○ OPN

LNP model:
— WT ON-S
— WT OFF-S
— OPN ON-S
— OPN OFF-S

(legend on next page)

population). The best match to the WT behavioral data is obtained with a memory duration of 320 ms. We locked this parameter for all four versions of the ideal observer model (WT ON-S, WT OFF-S, OPN ON-S, and OPN OFF-S model) so that there were no free parameters in the predictions for the OPN mice. Figure 4L compares the behavioral data for WT and OPN mice with the respective ideal observer model predictions. In WT mice, behavioral performance closely paralleled the model predictions for both ON-S and OFF-S RGCs. Strikingly, however, in OPN mice with the clear asymmetry between ON-S and OFF-S RGC sensitivities, behavior paralleled the model predictions for the less sensitive ON-S cells, although the OFF-S cells would have allowed even 4-fold higher visual sensitivity. The sensitivity difference between the WT ON-S and OPN ON-S RGC model predictions is robust against large changes in the memory component of the models, as is that between the WT OFF-S and OPN OFF-S ideal-observer model predictions (Figure 4L inset, see Figure S8 for a detailed analysis of model robustness). These results show that behavior correlates strongly with the population code originating from the less sensitive ON-S RGCs even though the population code originating from the OFF-S RGCs would have allowed significantly higher visual sensitivity.

DISCUSSION

Our results indicate that behavior at its sensitivity limit relies on the spike responses of ON-S RGCs, even when the gaps in the high tonic firing rates of OFF-S RGCs would carry more information about the weakest light increments. The results reveal three principles of what limits our capability to detect the weakest light signals and how the brain integrates information across parallel retinal outputs provided by ~40 different RGC types (Baden et al., 2016; Bae et al., 2018; Rheaume et al., 2018).

First, together with an earlier paper (Ala-Laurila and Rieke, 2014) on the primate retina, our results suggest that the absolute sensitivity of vision is mechanistically limited by nonlinear signal processing in the retinal ON pathway. In our experiments, behavior gets very close to the fundamental limit defined by the optimal readout of the ON-S RGCs population code across time. The ON pathway provides the brain with a more reliable but less sensitive readout of the weakest light inputs than the linear and noisier OFF pathway (Ala-Laurila and Rieke, 2014). Here, we show that the brain relies on this thresholded, nonlinear readout by the ON pathway at the sensitivity limit of vision.

Second, our results imply that the brain does not exploit the total information content present in the spike trains of all types of RGCs but relies on feature-specific information streams even at the absolute visual threshold. This is an important finding, since it is currently not known how the brain integrates visual information from distinct, parallel outputs of the several tens of recently identified RGC types contributing to vision at higher light levels. At least at the sensitivity limit of vision, the decoding principles of the brain do not produce the optimal solution predicted by information theory. This result provides a unique basis for

Figure 4. Ideal Observer Analysis Based on ON-S and OFF-S RGC Population Spike Trains in WT and OPN Mice

(A) Schematic of the ideal observer analysis: (1) the stimulus projections (green spot) on retinal ganglion cell mosaics (gray circles) were estimated from tracked mouse trajectories, (2) the RGC population responses (ON-S or OFF-S mosaics) were predicted using a time-space separable linear-nonlinear Poisson (LNP) model, and (3) the ideal observer relied on the population spike trains of RGCs and their relation to where the mouse was looking (STAR Methods) for optimal decisions about the stimulus location in behavioral experiments.

(B) Example spike rasters (top), PSTHs (bottom), and LNP model fits (orange lines) are shown for one OPN ON-S RGC (at three different light intensities, R*/rod/flash): 0.055, 0.082, and 0.12; 16.7-ms flashes, 200 μm spot diameter).

(C) The same as (B) for one OPN OFF-RGC (R*/rod/flash): 0.020, 0.034, and 0.058.

(D) Average temporal filters (left panel) for WT OFF-S (n = 21), ON-S (n = 22), OPN OFF-S (n = 14), and ON-S (n = 19) RGCs. Average intensity-response curves (right panel) for WT and OPN OFF and ON-S RGCs versus model predictions (orange). All curves were normalized relative to an intensity (I_C) eliciting a criterion response of four spikes relative to the baseline. Sp. count, spike count; Rel. int., relative intensity (I/I_C).

(E) Spatial filter exemplified for the same OPN ON-S RGC as in (B). The filter was obtained by fitting a symmetric Gaussian (orange) to the response amplitudes obtained by presenting light spots (200-μm spot, 50-ms flash, 0.37 R*/rod/flash) at different locations (inset: crosses indicate different spot centers) relative to the RGC soma. Responses in the insets are average responses (n = 5–50) corresponding to different radiuses from the receptive field (RF) center.

(F) The same as (E) but shown for the OPN OFF-S RGC (the same cell as in C).

(G) Mean spatial RFs shown for WT OFF-S (n = 17), ON-S (n = 15), OPN OFF-S (n = 16), and ON-S (n = 15) RGCs (no statistical differences between the means; p = 0.4, one-way ANOVA).

(H) The time-space separable LNP model fitted in (B) and (E) was validated for the same OPN ON-S RGC by predicting responses to a moving spot crossing the spatial RF at a speed of 2,000 μm/s (median speed from tracked behavioral data). Spike raster (top), PSTH (black, bottom), model (orange); 1.0 R*/rod/s; 200-μm spot.

(I) The same as (H) for OPN OFF-S (0.43 R*/rod/s; the same RGC as in C and F).

(J) Mean predictive performance of the model for a moving-spot stimulus for the population data of RGCs quantified by the signal power explained (see also Figure S6 for other measures): WT OFF-S (n = 11); WT ON-S (n = 12); OPN OFF-S (n = 12); OPN ON-S (n = 13).

(K) Comparison of WT visually guided behavior (open symbols) with an ideal observer model for WT ON-S RGCs with different memory durations with perfect access to the RGC spike code. Inf, average performance across all WT mice (n = 9) with a memory lasting across the entire swimming trajectory (median swimming time = 7 s; see also Figure 3G). WT OFF-S ideal observer had very similar performance (as shown in L).

(L) Comparison of WT and OPN mouse behavioral data (same data as in Figure 3H) with the ON-S and OFF-S versions of the ideal observer model predictions for WT and OPN strains (model memory duration = 320 ms, corresponding to the best fit between WT RGCs and behavior, see K). The predicted shift (Δ; estimated in the range 0.25–0.75 of fraction of correct choices) in behavioral performance for OPN mice in relation to WT mice as estimated from the ideal observer models relying on the ON-S RGC mosaic (dark blue arrow) or the OFF-S RGC mosaic (light blue arrow), respectively. Inset: Δ shown for ON-S (dark blue) and OFF-S (light blue) mosaics using different model memory durations. The dashed line shows the measured relative shift in behavioral sensitivity (OPN versus WT) as quantified in Figure 3H. All errors bars are SEMs.

See also Figures S2 and S5–S8.

future experiments aiming to unravel the decoding principles of the brain across different RGC outputs in conditions where more complex behaviors and retinal computations take place. Our finding is also robust against the possibility that a rare RGC type might be equally or more sensitive than alpha RGCs (Figures 2F and 2G). Just as the results show that the high-sensitivity information of the OFF-S RGCs is not utilized for behavioral decisions, the results would also imply that if any other rare, high-sensitive RGC type exists, then its spike information would also not be utilized optimally.

Third, our results are in line with the idea that the gaps in the firing of OFF-S RGCs are not used for behavioral decisions related to detecting light increments. Thus, behavior at the sensitivity limit of vision does not utilize the maximum information content present in the spike trains but instead relies on information presented in the form of increased spiking. It will be intriguing to see in future studies whether this is a more general principle across different behavioral paradigms. Along these lines of thinking, the OFF-S RGCs are likely to have a key role in decrement detection, as they send spikes in response to negative contrast. These principles are of key interest in the light of recent data indicating that visual information from the ON and OFF pathways is organized asymmetrically at the level of cortical circuits (Lee et al., 2016) and suggesting that the ON-OFF asymmetries could relate to a more fundamental design principle in sensory information processing.

Together, our results show the crucial importance of very precise quantitative linking between particular neural circuit functions and animal behavior for understanding how the brain decodes sensory information; i.e., understanding the neural blueprint. As a larger body of such evidence across different circuits and behavioral paradigms becomes available, it can lead to an entirely new level of resolution in understanding the information processing strategies of the brain.

STAR★METHODS

Detailed methods are provided in the online version of this paper and include the following:

- KEY RESOURCES TABLE
- LEAD CONTACT AND MATERIALS AVAILABILITY
- EXPERIMENTAL MODEL AND SUBJECT DETAILS
  - ○ Mice
- METHOD DETAILS
  - ○ Tissue preparation and solutions
  - ○ Histology
  - ○ Light stimuli
  - ○ Conversion of intensities to photoisomerizations
  - ○ Suction electrode recordings
  - ○ Ganglion cell recordings
  - ○ Behavioral measurements
  - ○ Pupil measurements
  - ○ Tracking of mouse body position and head direction
  - ○ Eye movement recordings
  - ○ Estimation of stimulus location on the retina
  - ○ Ideal observer model
  - ○ Data analysis
- QUANTIFICATION AND STATISTICAL ANALYSIS
- DATA AND CODE AVAILABILITY

AUTHOR CONTRIBUTIONS

L.S., D.T., J.T., N.M., and P.A.-L. designed and performed experiments. T.T. developed the methodology for mouse tracking. A.S., T.T., and J.W. developed the methodology for mouse eye tracking. L.S., D.T., J.T., T.T., J.W., and P.A.-L. analyzed data and wrote the manuscript.

REFERENCES

Aho, A.C., Donner, K., Hydén, C., Larsen, L.O., and Reuter, T. (1988). Low retinal noise in animals with low body temperature allows high visual sensitivity. Nature 334, 348–350.

Aho, A.C., Donner, K., Helenius, S., Larsen, L.O., and Reuter, T. (1993a). Visual performance of the toad (Bufo bufo) at low light levels: retinal ganglion cell responses and prey-catching accuracy. J. Comp. Physiol. A Neuroethol. Sens. Neural Behav. Physiol. 172, 671–682.

Aho, A.C., Donner, K., and Reuter, T. (1993b). Retinal origins of the temperature effect on absolute visual sensitivity in frogs. J. Physiol. 463, 501–521.

Ala-Laurila, P., and Rieke, F. (2014). Coincidence detection of single-photon responses in the inner retina at the sensitivity limit of vision. Curr. Biol. 24, 2888–2898.

Ala-Laurila, P., Donner, K., Crouch, R.K., and Cornwall, M.C. (2007). Chromophore switch from 11-cis-dehydroretinal (A2) to 11-cis-retinal (A1) decreases dark noise in salamander red rods. J. Physiol. 585, 57–74.

Azevedo, A.W., and Rieke, F. (2011). Experimental protocols alter phototransduction: the implications for retinal processing at visual threshold. J. Neurosci. *31*, 3670–3682.

Azevedo, A.W., Doan, T., Moaven, H., Sokal, I., Baameur, F., Vishnivetskiy, S.A., Homan, K.T., Tesmer, J.J., Gurevich, V.V., Chen, J., and Rieke, F. (2015). C-terminal threonines and serines play distinct roles in the desensitization of rhodopsin, a G protein-coupled receptor. eLife *4*, 1–22.

Baden, T., Berens, P., Franke, K., Román Rosón, M., Bethge, M., and Euler, T. (2016). The functional diversity of retinal ganglion cells in the mouse. Nature *529*, 345–350.

Bae, J.A., Mu, S., Kim, J.S., Turner, N.L., Tartavull, I., Kemnitz, N., Jordan, C.S., Norton, A.D., Silversmith, W.M., Prentki, R., et al.; Eyewirers (2018). Digital museum of retinal ganglion cells with dense anatomy and physiology. Cell *173*, 1293–1306.e19.

Bar-Shalom, Y., Daum, F., and Huang, J. (2009). The probabilistic data association filter. IEEE Control Syst. *29*, 82–100.

Baylor, D.A., Lamb, T.D., and Yau, K.W. (1979). The membrane current of single rod outer segments. J. Physiol. *288*, 589–611.

Bleckert, A., Schwartz, G.W., Turner, M.H., Rieke, F., and Wong, R.O. (2014). Visual space is represented by nonmatching topographies of distinct mouse retinal ganglion cell types. Curr. Biol. *24*, 310–315.

Bulat, A., and Tzimiropoulos, G. (2016). Human pose estimation via convolutional part heatmap regression. In Computer Vision – ECCV 2016: 14th European Conference Amsterdam, the Netherlands, October 11–14, 2016, Proceedings, Part VII, B. Leibe, J. Matas, N. Sebe, M. Welling, eds. (Springer International Publishing AG), pp. 717–732.

Burns, M.E., Mendez, A., Chen, J., and Baylor, D.A. (2002). Dynamics of cyclic GMP synthesis in retinal rods. Neuron *36*, 81–91.

Carter-Dawson, L.D., and LaVail, M.M. (1979). Rods and cones in the mouse retina. I. Structural analysis using light and electron microscopy. J. Comp. Neurol. *188*, 245–262.

Chichilnisky, E.J., and Rieke, F. (2005). Detection sensitivity and temporal resolution of visual signals near absolute threshold in the salamander retina. J. Neurosci. *25*, 318–330.

Cornwall, M.C., Jones, G.J., Kefalov, V.J., Fain, G.L., and Matthews, H.R. (2000). Electrophysiological methods for measurement of activation of phototransduction by bleached visual pigment in salamander photoreceptors. Methods Enzymol. *316*, 224–252.

Dolan, R.P., and Schiller, P.H. (1989). Evidence for only depolarizing rod bipolar cells in the primate retina. Vis. Neurosci. *2*, 421–424.

Dunn, F.A., and Rieke, F. (2008). Single-photon absorptions evoke synaptic depression in the retina to extend the operational range of rod vision. Neuron *57*, 894–904.

Field, G.D., Sampath, A.P., and Rieke, F. (2005). Retinal processing near absolute threshold: from behavior to mechanism. Annu. Rev. Physiol. *67*, 491–514.

Fu, Y., Kefalov, V., Luo, D.G., Xue, T., and Yau, K.W. (2008). Quantal noise from human red cone pigment. Nat. Neurosci. *11*, 565–571.

Gjorgjieva, J., Sompolinsky, H., and Meister, M. (2014). Benefits of pathway splitting in sensory coding. J. Neurosci. *34*, 12127–12144.

Govardovskii, V.I., Fyhrquist, N., Reuter, T., Kuzmin, D.G., and Donner, K. (2000). In search of the visual pigment template. Vis. Neurosci. *17*, 509–528.

Grimes, W.N., Schwartz, G.W., and Rieke, F. (2014). The synaptic and circuit mechanisms underlying a change in spatial encoding in the retina. Neuron *82*, 460–473.

Hayes, J.M., and Balkema, G.W. (1993). Elevated dark-adapted thresholds in hypopigmented mice measured with a water maze screening apparatus. Behav. Genet. *23*, 395–403.

Hecht, S., Shlaer, S., and Pirenne, M.H. (1942). Energy, quanta, and vision. J. Gen. Physiol. *25*, 819–840.

Henriksson, J.T., Bergmanson, J.P., and Walsh, J.E. (2010). Ultraviolet radiation transmittance of the mouse eye and its individual media components. Exp. Eye Res. *90*, 382–387.

Jeon, C.-J., Strettoi, E., and Masland, R.H. (1998). The major cell populations of the mouse retina. J. Neurosci. *18*, 8936–8946.

Kent, A., and Williams, J.G. (1991). Encyclopedia of Computer Science and Technology: Volume 25, Supplement 10: Applications of Artificial Intelligence to Agriculture and Natural Resource Management to Transaction Machine Architectures (CRC Press).

Kuo, S.P., Schwartz, G.W., and Rieke, F. (2016). Nonlinear spatiotemporal integration by electrical and chemical synapses in the retina. Neuron *90*, 320–332.

LeCun, Y., Bengio, Y., and Hinton, G. (2015). Deep learning. Nature *521*, 436–444.

Lee, K.S., Huang, X., and Fitzpatrick, D. (2016). Topology of ON and OFF inputs in visual cortex enables an invariant columnar architecture. Nature *533*, 90–94.

Lyubarsky, A.L., Daniele, L.L., and Pugh, E.N.J., Jr. (2004). From candelas to photoisomerizations in the mouse eye by rhodopsin bleaching in situ and the light-rearing dependence of the major components of the mouse ERG. Vision Res. *44*, 3235–3251.

Meyer, A.F., Poort, J., O'Keefe, J., Sahani, M., and Linden, J.F. (2018). A head-mounted camera system integrates detailed behavioral monitoring with multi-channel electrophysiology in freely moving mice. Neuron *100*, 46–60.e7.

Murphy, G.J., and Rieke, F. (2006). Network variability limits stimulus-evoked spike timing precision in retinal ganglion cells. Neuron *52*, 511–524.

Murphy, G.J., and Rieke, F. (2011). Electrical synaptic input to ganglion cells underlies differences in the output and absolute sensitivity of parallel retinal circuits. J. Neurosci. *31*, 12218–12228.

Naarendorp, F., Esdaille, T.M., Banden, S.M., Andrews-Labenski, J., Gross, O.P., and Pugh, E.N.J., Jr. (2010). Dark light, rod saturation, and the absolute and incremental sensitivity of mouse cone vision. J. Neurosci. *30*, 12495–12507.

Nirenberg, S. (2012). Strategies for finding neural codes. In Visual Population Codes, N. Kriegeskorte and G. Kreiman, eds. (The MIT Press), pp. 53–69.

Oommen, B.S., and Stahl, J.S. (2008). Eye orientation during static tilts and its relationship to spontaneous head pitch in the laboratory mouse. Brain Res. *1193*, 57–66.

Payne, H.L., and Raymond, J.L. (2017). Magnetic eye tracking in mice. eLife *6*, e29222.

Remtulla, S., and Hallett, P.E. (1985). A schematic eye for the mouse, and comparisons with the rat. Vision Res. *25*, 21–31.

Rheaume, B.A., Jereen, A., Bolisetty, M., Sajid, M.S., Yang, Y., Renna, K., Sun, L., Robson, P., and Trakhtenberg, E.F. (2018). Single cell transcriptome profiling of retinal ganglion cells identifies cellular subtypes. Nat. Commun. *9*, 2759.

Rieke, F. (2000). Mechanisms of single-photon detection in rod photoreceptors. Methods Enzymol. *316*, 186–202.

Sahani, M., and Linden, J.F. (2003). How linear are auditory cortical responses. Adv. Neural Inf. Process. Syst. *15*, 125–132.

Sanes, J.R., and Masland, R.H. (2015). The types of retinal ganglion cells: current status and implications for neuronal classification. Annu. Rev. Neurosci. *38*, 221–246.

Schiller, P.H. (1982). Central connections of the retinal ON and OFF pathways. Nature *297*, 580–583.

Schiller, P.H. (1992). The ON and OFF channels of the visual system. Trends Neurosci. *15*, 86–92.

Schiller, P.H. (2010). Parallel information processing channels created in the retina. Proc. Natl. Acad. Sci. USA *107*, 17087–17094.

Schiller, P.H., Sandell, J.H., and Maunsell, J.H. (1986). Functions of the ON and OFF channels of the visual system. Nature *322*, 824–825.

Schoppe, O., Harper, N.S., Willmore, B.D.B., King, A.J., and Schnupp, J.W.H. (2016). Measuring the performance of neural models. Front. Comput. Neurosci. *10*, 10.

Stahl, J.S. (2004). Using eye movements to assess brain function in mice. Vision Res. *44*, 3401–3410.

Takeshita, D., Smeds, L., and Ala-Laurila, P. (2017). Processing of single-photon responses in the mammalian On and Off retinal pathways at the sensitivity limit of vision. Philos. Trans. R. Soc. Lond. B Biol. Sci. *372*, 20160073.

Toda, K., Bush, R.A., Humphries, P., and Sieving, P.A. (1999). The electroretinogram of the rhodopsin knockout mouse. Vis. Neurosci. *16*, 391–398.

van Wyk, M., Wässle, H., and Taylor, W.R. (2009). Receptive field properties of ON- and OFF-ganglion cells in the mouse retina. Vis. Neurosci. *26*, 297–308.

Wark, B., Fairhall, A., and Rieke, F. (2009). Timescales of inference in visual adaptation. Neuron *61*, 750–761.

Wässle, H., and Boycott, B.B. (1991). Functional architecture of the mammalian retina. Physiol. Rev. *71*, 447–480.

Yao, X., and Field, G.D. (2019). Inhibition controls receptive field size, sensitivity, and response polarity of direction selective ganglion cells near the threshold of vision. bioRxiv. https://doi.org/10.1101/683961.

STAR★METHODS

KEY RESOURCES TABLE

REAGENT or RESOURCE	SOURCE	IDENTIFIER
Chemicals, Peptides, and Recombinant Proteins		
Ames	Sigma-Aldrich	A1420
HiLyte Fluor 750 hydrazide	AnaSpec	AS-81268
Eosin B (Certistain)	Merck	115934
Hematoxylin (Certistain)	Merck	115938
Pilocarpine hydrochlorid 20mg/ml (Isopto Carpine)	Novartis Finland Oy	Vnr 53 60 37
Experimental Models: Organisms/Strains		
Mouse: Rho::OPN1LW	Fu et al., 2008	N/A
C57BL/6J	Charles River	JAX C57BL/6J
Software and Algorithms		
MATLAB (version: R2016a)	The Mathworks	https://se.mathworks.com/products/matlab.html
OriginPro (version: 2018b)	OriginLab	https://www.originlab.com
Symphony versions: 1.0 (suction pipette rig); 1.2.1.0 and onward (patch clamp rigs)	Symphony-DAS; Ala-Laurila Lab	https://github.com/Symphony-DAS/; https://github.com/ala-laurila-lab/
ImageJ (version: 1.47)	NIH	https://imagej.nih.gov/ij/
Andor iQ3	Oxford Instruments	https://andor.oxinst.com/products/iq-live-cell-imaging-software/andor-iq3
Python (version: 3.6)	Python Software Foundation	https://www.python.org
OpenCV (version: 3.4)	OpenCV team	https://opencv.org/
NumPy (version: 1.16)	NumPy developers	https://www.numpy.org/
SciPy (version: 1.2)	SciPy developers	https://www.scipy.org/
PySide2 (version: 5.6)	Qt Project	https://wiki.qt.io/PySide
TensorFlow (version: 1.12 GPU)	Google Brain Team	https://www.tensorflow.org
VirtualDub (version: 1.10.4)	virtualdub.org	http://virtualdub.org
Java (version: SE 7)	Oracle	https://www.oracle.com/index.html
Micro-Manager (version 1.4.22)	Open Imaging	https://micro-manager.org
Other		
Microscope for rod recordings (suction pipette rig)	Zeiss	Invertoscope D
Microscope for ganglion cell recordings (patch clamp rig 1)	Nikon	Eclipse FN1
Microscope for ganglion cell recordings (patch clamp rig 2)	Scientifica	SliceScope Pro 3000
Amplifier for rod recordings (suction pipette rig)	Axon Instruments / Molecular Devices	Axopatch 200B
Amplifier for ganglion cell recordings (patch clamp rig 1 and 2)	Axon Instruments / Molecular Devices	MultiClamp 700B
Light Projector (patch clamp rig 2)	Texas Instruments	DLP LightCrafter 4500
Excitation light source for epifluorescence (patch clamp rig 1)	Excelitas Technologies	X-Cite 120Q
Camera for fluorescence imaging (patch clamp rig 1)	Andor technology, Oxford Instruments	iXon Ultra 897 EMCCD
Excitation light source for epifluorescence (patch clamp rig 2)	CoolLED	CoolLED pE-4000
Camera for fluorescence imaging (patch clamp rig 2)	Andor technology, Oxford Instruments	Zyla 4.2 PLUS sCMOS

Continued

REAGENT or RESOURCE	SOURCE	IDENTIFIER
Camera for tracking mouse behavior and measuring pupil size	Watec	Wat-902H2 Ultimate
Camera for tracking mouse eye movements	Andor technology, Oxford Instruments	Zyla 4.2 PLUS sCMOS
Microscope used for histology	Olympus	BX-61TRF
Optometer for light calibrations	UDT Instruments	S470 & S450 with 268R sensor
Spectrometer for spectral irradiance measurements of light stimuli	Ocean Optics	JAZ-COMBO

LEAD CONTACT AND MATERIALS AVAILABILITY

Further information and requests for resources and reagents should be directed to and will be fulfilled by the Lead Contact, Petri Ala-Laurila (petri.ala-laurila@helsinki.fi).

EXPERIMENTAL MODEL AND SUBJECT DETAILS

Mice
Wild-type (WT) mice and mice carrying a transgene containing the human red cone opsin gene (OPN1LW) under the control of the mouse Rhodopsin (Rho) promoter (Fu et al., 2008) were used for all of the experiments (at the age of 5–16 weeks). The Rho::OPN1LW allele was maintained in a homozygous state. This transgenic mouse line is referred to as OPN. WT mice were from the same "mixed" background (C57BL/6J & OPN lines crossed). The genotypes were confirmed by PCR. Mice from the 2nd–5th generations were used for all the experiments. The key experimental parameters (ON-S and OFF-S RGC thresholds, L-cone pigment expression level, the single-photon response amplitude in rods and the sensitivity of rods) were monitored across mouse generations throughout the study. No systematic changes were observed.

The mice were dark-adapted before all experiments: overnight for RGC and rod recordings, and for 2–3 hours for behavioral experiments. For rod and RGC recordings, the mice were sacrificed by rapid cervical dislocation, and their eyes were enucleated, hemisected, and stored at $32 \pm 1°C$ in oxygenated (95% O_2, 5% CO_2) Ames solution (Sigma, A-1420; osmolality adjusted to 280 ± 2 mOsm/kg). This and all subsequent procedures were performed under infrared illumination (> 900 nm) using night vision goggles (PVS-7-1600, B.E. Meyers) and IR pocket scopes (D7200-I-1600, B.E. Meyers) attached to the dissection microscope. Behavioral experiments were carried out in IR illumination using night vision goggles. Rod and RGC recordings were made in complete darkness. The mice were raised under 12/12 hour light/dark cycle (white light: ~300 lux). All experiments as well as mouse training for behavioral experiments were done during the subjective day time of this cycle. All animal procedures were performed according to the protocols approved by the Regional State Administration Agency for Southern Finland. Sample sizes were not determined prior to the experiments, and the investigators were not blinded to the mouse strains.

METHOD DETAILS

Tissue preparation and solutions
Rod photoreceptor preparations and flat mount preparations for RGC recordings followed previously described procedures (for rod procedures, see Azevedo et al., 2015; for RGC procedures, see Murphy and Rieke, 2011; Ala-Laurila and Rieke, 2014). Briefly, pieces of the retina were flattened on poly-D-lysine-coated glass coverslips (12-mm; VWR, Corning) with the photoreceptor layer down and placed on the microscope (Eclipse FN 1, Nikon for RGC threshold recordings; SliceScope Pro 3000, Scientifica for RGC recordings needed for the LNP model). For rod recordings, a piece of the retina was chopped in ~500 μL of oxygenated Ames solution on a Sylgard-coated (SYLG184, WPI) dish and the resulting cell suspension was transferred to the recording chamber on an inverted microscope (Invertoscope D, Zeiss). The cells were allowed to adhere to the bottom of the chamber for 8–10 min before the perfusion was started. All preparations were perfused at $32 \pm 1°C$ with oxygenated Ames medium (flow rate: ~8 ml/min for RGC recordings; ~2 ml/min for rod recordings). The electrodes for RGC recordings (~3 MΩ) and for rod recordings (~3–4 MΩ; fire-polished to an inner diameter of ~1.5 μm) were filled with Ames. In some of the rod experiments, Ames buffered with HEPES (pH = 7.4) (Azevedo and Rieke, 2011) was used to fill the electrodes. No differences were found in the reported response parameters between these two recording conditions.

Histology
Histological preparations were made using the eyes of the mice that were used in the behavioral experiments (~1 month after the behavioral experiments). Both freshly dissected eyes of the euthanized mouse were fixed in Bouin at +21°C for 24 hours.

The eyes were further processed in 70% ethanol (2 × 2 hours; replacing the ethanol between treatments) and in 94% ethanol (2 × 2 hours). The eyes were then left in 94% ethanol overnight. The fixation process continued as follows: 94% ethanol + butanol (1:1, 2 × 2 hours), butanol (overnight), butanol (wash, 2–4 hours) and paraffin (overnight at +58°C). The paraffin was changed 2–3 times before the eyes were embedded in paraffin. The eyes were stored at +4°C before sagittal sections (~5 μm in thickness) were made with a microtome (Jung Biocut 2035, Leica). The tissue was stained with hematoxylin and eosin. Images of the sections were taken with a digital camera (Olympus DP73) mounted to the microscope (Olympus BX-61TRF).

Light stimuli
Calibrated light stimuli centered on the target cell were delivered in both rod and RGC recordings: Rods were stimulated using a 590-nm LED and 20-ms flashes of a spatially uniform spot (~580 μm in diameter). For rod spectral sensitivity measurements, three different LEDs were used (peaks at 590 nm, 660 nm, and 740 nm). RGCs were stimulated using 20-ms flashes and a spot stimulus (~580 μm in diameter) delivered from a LED (peak at ~470 nm) in 2AFC threshold measurements. For LNP model training data, we used a DLP projector (912 × 1140 pixels; 1.8 μm/pixel on retinal surface; 60 Hz frame rate; blue LED spectral peak ~450 nm; Texas Instruments, LightCrafter 4500) to present uniform light spots of various sizes (200–600 μm) and durations (17–300 ms). For LNP model validation data, we used the same DLP projector to create a moving spot stimuli (200 μm in diameter; speed set to 2000 μm/s corresponding to the median speed of the retinal projection as estimated based on animal tracking in behavioral experiments). The stimulus light was focused on the preparation (photoreceptor) plane by a microscope condenser in both rod and RGC recordings. In RGC recordings, the retina was stimulated from the photoreceptor side. In behavioral experiments, the stimuli consisted of a circular plexiglass-diffusor window (~40 mm in diameter) located at the end of each corridor in the water maze (see Figure 3A). One of the windows (the stimulus window) was continuously illuminated by a green LED (peak at 515 nm) and narrow-band filtered with a 512-nm interference filter (~10-nm transmission bandwidth) during each experimental trial. The light intensity was set by neutral density filters and by controlling the current driving the LEDs. Light intensities were calibrated with an optometer (Models S470 & S450 with 268R sensor, UDT Instruments) and the spectral irradiances of stimuli were measured (Jaz spectrometer, Ocean Optics).

Conversion of intensities to photoisomerizations
Rod and RGC measurements
Stimulus intensities are given in terms of isomerizations per rod (R*/rod), based on the measured LED spectral output, the rod spectral sensitivity as estimated from a pigment template (Govardovskii et al., 2000), and the rod collecting areas (A_c) measured using suction pipette recordings. We used A_c = 0.63 μm^2 for WT and A_c = 0.41 μm^2 for OPN rods (see section Data analysis, below).
Behavioral measurements
Light intensities from the stimulus window were measured in the center of the water maze, where the mouse eye (cornea) would be at the beginning of each experimental trial. These measurements were converted into isomerization rates in rods by computing the size of the projected stimulus spot on the retinal surface (~170 μm in diameter), the total flux of photons reaching the retina and by using the measured collecting areas of WT and OPN mouse rods. For these calculations we used the optical parameters of the mouse eye (Remtulla and Hallett, 1985). The calculations followed previously described procedures (Lyubarsky et al., 2004; Naarendorp et al., 2010) and are described below.

The power measurements obtained in the center of the maze were converted into a corneal photon flux, ϕ (s^{-1}):

$$\phi = \frac{\lambda P_{center}}{hc}, \tag{1}$$

where P_{center} is the stimulus light power measured at the center of the maze, h is Planck's constant, c is the speed of light and λ is the wavelength of the stimulus light (512 nm). All wavelength-dependent parameter values have been selected for this stimulus wavelength. The corneal photon flux (ϕ) was converted to the corneal photon flux density (F_{cornea}) by:

$$F_{cornea} = \frac{\phi}{A_{sensor}}, \tag{2}$$

where A_{sensor} is the area of the radiometric sensor covered by a uniform photon flux (1 cm^2 in our case). For conversion of F_{cornea} into the photon flux density at the level of the retina (F_{retina}), the area of the dark-adapted pupil (A_{pupil}), the projection area of the stimulus on the retina (A_{retina}) and the loss factors in the mouse's eye were estimated. The measurements of A_{pupil} are described in the section Pupil measurements below and the results are shown in Figure 3C. For A_{retina}, we assumed that the mouse was looking at the stimulus from the center of the maze. The visual angle (β) can be calculated as:

$$\beta = 2 \left[\tan^{-1} \left(\frac{r_{stimulus}}{D} \right) \right] \tag{3}$$

where $r_{stimulus}$ is the radius of the stimulus (20 mm) and D is the distance between the stimulus and the mouse (in our case 390 mm, see Figure S2B). The mouse retina was approximated as a hemisphere (Lyubarsky et al., 2004) with a radius (r_{retina}) of 1.7 mm and with the center corresponding to the posterior nodal point of the eye optics (Lyubarsky et al., 2004; Remtulla and Hallett, 1985). The

projection of the stimulus diameter onto the retinal surface (s_{retina}) is estimated as:

$$s_{retina} = \frac{\beta}{180°}\ \pi\ r_{retina} \tag{4}$$

and the area (A_{retina}) as

$$A_{retina} = \pi \left(\frac{s_{retina}}{2}\right)^2 \tag{5}$$

In our case, the numerical values were: s_{retina} = 170 μm and A_{retina} = 22700 μm^2. These values were used to convert F_{cornea} to the retinal photon flux density (F_{retina}) by:

$$F_{retina} = \frac{F_{cornea}\ A_{pupil}}{A_{retina}}\ \tau_{media}, \tag{6}$$

where τ_{media} is the light transmittance of the ocular media (0.55; Henriksson et al., 2010), and A_{pupil} is the pupil area as measured in Figure 3C. We estimated the number of photoisomerizations per rod by multiplying F_{retina} by the collecting area for a rod at its peak wavelength (A_c) and by the relative absorption factor for mouse rod rhodopsin at the stimulus wavelength 512 nm ($R_{512\ nm}$). We estimated $R_{512\ nm}$ to be 0.93 based on the Govardovskii template (Govardovskii et al., 2000; assuming the wavelength of maximum absorbance, λ_{max} = 497 nm (Toda et al., 1999). Light intensity (I) in photoisomerizations per rod per second (R*/rod/s) was thus finally calculated as:

$$I = \frac{F_{cornea}A_{pupil}}{A_{retina}}\ \tau_{media}\ A_c R_{512nm} \tag{7}$$

For the ideal observer, the photoisomerization rates were calculated at each point along the swimming route. The calculations were performed as above, but with the following modifications. The stimulus power at the center of the maze (P_{center}) was replaced with the stimulus power measured at different locations of the maze. The effective area of the pupil was estimated by weighting the full area of the pupil (A_{pupil}) by the cosine of the angle between the optical axis and a ray originating from the stimulus center (Naarendorp et al., 2010). The size of the stimulus projection was obtained by projecting the stimulus window's contour onto the retina and by calculating the area of the projection on a spherical surface (see the section Estimation of stimulus location on the retina below).

Suction electrode recordings

The membrane current of a rod was recorded by drawing its outer segment projecting from a small piece of the retina to a tight-fitting glass pipette following previously described procedures (Baylor et al., 1979; Azevedo et al., 2015). Rods were selected for the recording if they appeared morphologically sound and if their dark-current exceeded ~8 pA. The cells were visualized using IR light (peak at 940 nm) and a CCD camera (LCL-902HS, Watec) attached to the microscope. Signals were amplified and low-pass filtered at 5 kHz (Axopatch 200B, 4-pole Bessel, Molecular Devices) followed by low-pass filtering at 50 Hz (8-pole Bessel, Frequency Devices). A Humbug noise eliminator (QuestScientific, Canada) was used to minimize 50 Hz noise. The data were digitized at 10 kHz (ITC18, HEKA) for further analysis. The data were collected using the custom-written MATLAB-based stimulation and acquisition software Symphony (http://symphony-das.github.io). In all recordings, the quality of the recording was monitored by measuring the intensity–response relation (IR-relation) of the rod at 4–6 intensities (1–50 flashes at each intensity) throughout the recordings. Only data where the maximal response amplitude and half-saturating intensity remained within 20% of those measured at the beginning of each recording were included.

We used previously described protocols to measure the spectral sensitivity of rods (Ala-Laurila et al., 2007), single-photon response amplitude (Rieke, 2000), and the detection performance in the two-alternative forced choice task (Ala-Laurila and Rieke, 2014; Azevedo et al., 2015; see also the section Data analysis below). Briefly, for spectral sensitivity measurements, we measured the intensity needed to elicit the same criterion size response (see Figure 1C). Sequences of stimulation with 5–6 flash intensities at a reference wavelength (590 nm) were interleaved with series of 10–100 dim flashes at each of the two test wavelengths (660 nm and 740 nm; selected at the long-wavelength range of the spectrum to allow L-cone pigment contribution to be measured). Flash strengths were chosen to elicit responses with amplitudes < 25% of the maximal response in the linear range of the rod's intensity-response function. For single-photon response analysis, 30–100 flashes eliciting a small number of isomerizations in rods were delivered at one to three different intensities (typically in the range 0.6–2 R*/flash). For detection performance measurements, sequences of dim flashes (30–200 flash responses per intensity in the range 0.3–8 R*/rod/flash) were taken.

Ganglion cell recordings

Flat mount preparations were visualized using IR light (940 nm; turned off during electrical recordings) and a CCD camera (Wat-902H Ultimate, Watec) attached to the microscope. Signals were amplified (MultiClamp 700B, Molecular Devices), low-pass filtered (cut-off: 3kHz, 8-pole Bessel) and digitized at 10 kHz (ITC18, HEKA). The data were collected using Symphony (see above).

ON-S and OFF-S RGC measurements

All ON-S and OFF-S RGC recordings were made from visually and functionally identifiable ON-S or OFF-S alpha RGCs using cell-attached patch clamp technique (loose patch) to record the spiking activity. The RGCs were identified by their large soma size (~15–20 μm diameter) and characteristic responses to light steps from darkness (500-ms light step at 1–2 R*/rod/s; Murphy and Rieke, 2006; Wark et al., 2009; van Wyk et al., 2009). In some cases, the dendritic morphology of cells was verified by filling the cells with a fluorescent dye (HiLyte Fluor 750 hydrazide, AnaSpec, AS-81268) and imaging the cells (Andor iXon Ultra 897 EMCCD and Andor Zyla 4.2 PLUS sCMOS) following fluorescence excitation (peak at 740 nm; width 35nm, X-Cite 120Q, Excelitas Technologies and CoolLED pE-4000, CoolLED). The cell morphology was confirmed to be consistent with ON-S (Bleckert et al., 2014) or OFF-S alpha RGCs (van Wyk et al., 2009).

Full mosaic RGC measurements

A subset of the RGC recordings were made using full RGC mosaics to compare the sensitivity of ON-S and OFF-S alpha cells with the sensitivity of all other RGC types in the mouse retina. We targeted every RGC soma (~10–50 RGCs per mount; constrained by the recording duration: typically < 7 hours) next to an identified ON-S and/or OFF-S alpha cell (see above) and tested their sensitivity using the 2AFC framework (see below). We used an iterative protocol: First, all RGCs were categorized to two groups: those responding to a dim probe stimulus (500-ms light step, 1–10 R*/rod/s) and those that did not respond. The sensitivity of the responding cells was quantified using a sequence of flashes (20-ms; 4–7 intensities; 20–50 flashes per intensity), whereupon the intensity of the probe stimulus was elevated ~10-fold at a time and the procedure was repeated. The highest flash intensity tested was ~1000 R*/rod/flash. The quality of the preparation was checked by testing the ON-S and/or OFF-S RGC sensitivity repeatedly. Only mounts where alpha RGC sensitivity did not change markedly were kept. Our method provides the low-intensity bound for the sensitivity threshold of "other" RGC types, as only those RGCs that responded within the intensity range tested were included in the further analysis.

Behavioral measurements

The visual threshold of mice was determined by monitoring their ability to find a dim light spot in a black six-armed water maze in darkness using a six-alternative forced choice (6AFC) paradigm (Figure 3A; see also Hayes and Balkema, 1993). The body and head positions of the mice were monitored during the behavioral trials in IR light using a sensitive CCD camera attached above the maze (Wat-902H2 Ultimate, Watec; equipped with a 12VM412ASIR lens, Tamron) and our fully-automated, novel system for tracking mouse behavior. All experiments were recorded using open-source video capture software (VirtualDub 1.10.4, http://virtualdub.org) and stored on the computer in the AVI file format.

The mice were placed in the center of the maze in a transparent tube, and allowed to orient themselves for ~5 s (see Figure S1A-C). Then the transparent tube was removed allowing the mice to approach the stimulus light and/or other locations in the maze (see Figure 3A, D). The choice was defined as correct if the mice entered the right channel before going into any other channel (50% of the mouse's body entering the corridor used as the criterion). The mice were first trained (4 trials per day per mouse in dim ambient illumination, Figure 3A) to associate the stimulus light with an escape ramp from the water (~20°C) using an easily detectable light spot intensity (corresponding to 200 000 R*/rod/s; at the center of the maze). After training (for ~2 weeks) the mice made the right choice in ≥ 80% of the trials (Figure 3B). Thereafter, the mice (11 OPN: 5 males and 6 females, and 9 WT mice: 3 males, 6 females.; 4 trials per day) were tested at a sequence of intensities (0.0014–200 000 R*/rod/s, one intensity per day, ~4-week period) starting at the training intensity and decreasing the light intensity 2–10-fold each day until the mice made a choice completely randomly (1/6 = random selection). If the mouse did not enter the stimulus corridor within 45 s, it was removed from the maze. In such a case, it was considered that the mouse failed to locate the stimulus. The mice were taught to voluntarily climb from the ramp to the hand as they were removed from the maze to lower the stress level. Thereafter, they were put in a dry and heated cage for several minutes. The location of the stimulus light was randomized, the water was mixed, and the ramp was rinsed with water between the trials. There was a fan on top of the maze to obfuscate possible odorant cues. We also tested the maze for any biases in the *a priori* probabilities of choosing a particular corridor (Figures S1D-E). Female and male mice were handled separately and the sex order and the strain order were alternated every day.

At the end of the experimental series, the mice were re-tested at a high intensity to make sure that no changes had occurred in their ability to perform the task (Figure 3A top panel). We also tested that the visually-guided behavior and search strategy taking place only at the center of the maze gives a similar difference between the OPN and WT mouse strains than taking into consideration the behavior in the entire maze (Figure S4). Furthermore, we tested that the IR light used in behavioral experiments was dim enough not to cause any significant effects on visual sensitivity or RGC thresholds. We estimate that the IR light caused < 0.03 R*/rod/s background activity in the rods. This upper-limit estimate for background activity is within a factor of 3 from the estimated rate of spontaneous pigment activations in mouse rods (0.01 R*/rod/s, Burns et al., 2002; Fu et al., 2008).

Pupil measurements

The pupil sizes of the mice were determined in the dark in identical conditions to the experiments by monitoring their eyes using an IR-sensitive camera (WAT-902H2, Watec) connected to a macro lens (MLH-10X, Computar). The mouse (held by its tail) was aligned toward the camera, and the pupil areas were measured from single frames of the video recording. Pupil areas were measured from the same individuals that were used in behavioral experiments.

Tracking of mouse body position and head direction

We developed a fully automated markerless video tracking technology to quantify the body and head movements of freely swimming mice in a water maze in dim IR illumination (Video S1). Commercially available tracking solutions did not allow us to track either the mouse position or its head orientation in our experimental conditions. The challenge was related to the low contrast, as a black mouse needed to be detected against the black background of the water maze. This section demonstrates very briefly the key principles and the validation of our tracking system. A detailed methodological description of the tracking technology and its algorithms will be published in a separate technical paper (T.T. and P.A.-L., unpublished data).

The tracking system was fully automated and required no human intervention during the experiments. The system recognized all experimental stages (including the arrivals of mice in the maze) relying on object detection based on a convolutional neural network (LeCun et al., 2015), a finite-state machine (FSM) and a defined causality model of the experimental flow (Kent and Williams, 1991). Tracking included two steps. First, the mouse body was tracked using a probabilistic data association filter (PDAF; Bar-Shalom et al., 2009). This was needed to distinguish the contour of the mouse's body from random clutter (noise). Second, the head position and head orientation of the mouse was tracked using a shallow convolutional neural network and four Kalman filters. The neural network first estimated the positions of the head center, the nose, and the left and the right ear using body part heatmap regression (Bulat and Tzimiropoulos, 2016). The estimates were graded against a body-part-relation model and the best estimates were fed into the associated body-part tracking Kalman filters. The final head center position and nose direction were thus estimated based on the predictions obtained from the Kalman filters. The position of the water maze was automatically determined from the videos based on alignment markers on the maze to obtain tracking results in an absolute coordinate system (in mm relative to the center of the maze). Video tracking was implemented using the Python programing language (Python Software Foundation, https://www.python.org; version 3.6) and TensorFlow (Google Brain Team, https://www.tensorflow.org). The tracked mouse data were stored as HDF5 files, which contained all metadata regarding the experimental parameters and all data of mouse swimming tracks and head orientations. In addition to the original videos, another version with the tracking results overlaid was stored for later inspection.

We validated the estimates obtained automatically by the tracker in a separate set of experiments by comparing the automatically defined percent correct results to those obtained by watching videos using a test dataset consisting of 1300 mouse swimming trials. The results were identical within measurement error (the root-mean-square error between the two estimates < 0.03 fraction of correct choice).

Eye movement recordings

The eye-movements of freely-swimming mice were recorded at 100 frames/s (2048x2048 16-bit grayscale images) with a high-speed scientific CMOS camera (Andor Zyla 4.2+ sCMOS) placed ∼60 cm above the water maze. All eye movement recordings were made post-training using a separate group of 6 WT mice (2 males and 4 females) and 6 OPN mice (3 females and 3 males). The recordings were made in darkness at one stimulus intensity for both strains corresponding to ∼40% fraction of correct choices: 0.03 R*/rod/s (WT) and 0.3 R*/rod/s (OPN). The mice were treated with pilocarpine eye drops (Novartis, Isopto Carpine 20 mg/ml) 30 min prior to each experiment, as this contracted the pupils such that their areas were ∼60%–70% of those in darkness. This made the pupils discernable in the video recordings.

Our water maze setup considerably simplified the task of tracking eye movements, as swimming mice keep their heads in an upward-tilted position (Figure 3E and Figure S3A). This upward tilt made the eyes clearly visible from above during free swimming, and it thus allowed us to detect and track landmarks at various head and eye locations (Figure S3B and Video S2). Head orientation, eye corners, and pupil positions were extracted semi-automatically (as detailed below) within each frame. These data allowed us to determine the angular speeds of both head and eye movements: The head orientation was extracted from the ear and nose positions (localized using intensity-based clustering), the pupil by fitting an ellipse to its contour (least-squares), and the eye corners through manual labeling in each frame.

Compensatory eye-movements have traditionally been estimated in head-fixed mice, where head rotations are under the control of the experimenter (Stahl, 2004). This is not the case for freely-moving (swimming) mice, which move their heads continuously. We therefore took a similar approach as in Meyer et al. (2018), and extracted and analyzed head turn events occurring throughout the swimming trajectory. These events were obtained by extracting frame sequences of continuous head rotations over 50–250 ms, where the average angular speed was at least 15°/s. The first and last frame of one such head turn event is shown in Figure S3C, with the total displacement for both head and pupil (one eye) positions highlighted. Angular velocities were calculated for each frame by comparing the displacement in location between consecutive frames. For head rotations, the angular velocity was computed directly from the change in the orientation angles between frames, whereas eye angular velocities were extracted from relative changes in the distances between pupil and eye corners as (Figure S3D):

$$v_{eye} = \frac{\theta}{0.01s} = \frac{2 \sin^{-1}\left(\frac{\Delta d}{2r}\right)}{0.01s}, \tag{8}$$

where Δd is the relative pupil movement between frames and r is the radius of a spherical model of the eye (1.7 mm; Remtulla and Hallett, 1985). Both head orientation and Δd were low-pass filtered (20 Hz cutoff) prior to any velocity calculations. The data for each head turn event thus consisted of two vectors, one containing the angular velocities of the head and the other the angular velocities of the eye (Figure S3E). The data points in Figure 3E are mean velocities during each event.

Estimation of stimulus location on the retina

Each eye was described using a simple pinhole optical model with the pinhole placed 1.7 mm from the retina (Remtulla and Hallett, 1985). The retina, in turn, was modeled by distributing an approximately hexagonal grid of rods and ON-S or OFF-S RGCs on a spherical surface (Figure S2) that covered 200 degrees of the back of the eye (Lyubarsky et al., 2004). The rod density was set to 437 000 rods/mm^2 (Jeon et al., 1998), whereas the RGC density was set uniformly to 100 cells/mm^2 (average density of ON-S and OFF-S alpha RGCs; Bleckert et al., 2014). The spatial receptive field of each RGC was Gaussian shaped with a fixed radius of 150 μm (corresponding to 2σ in our Gaussian RF fits, see Figure 4G).

Stimulus projections relied on transforming stimulus coordinates between two coordinate systems: one maze coordinate system with its origin at the center of the maze, and a second retinal coordinate system with its origin at the pinhole of the optical model. A point (**p**) given in maze coordinates could thus be transformed to retinal coordinates using the following transformation:

$$\mathbf{p}_{retina} = \mathbf{M}\,\mathbf{p}_{maze}, \tag{9}$$

$$\mathbf{M} = \mathbf{R}_{stabilization}\,\mathbf{T}_{eye\ pos.}\ \mathbf{R}_{azimuth}\ \mathbf{R}_{elevation}\mathbf{R}_{head\ angle}\mathbf{T}_{head\ pos.}, \tag{10}$$

where $\mathbf{R}_{stabilization}$ accounts for stabilizing eye movements, $\mathbf{T}_{eye\ pos.}$ translates the origin from the center of the head to the pinhole, $\mathbf{R}_{azimuth}$ and $\mathbf{R}_{elevation}$ set the resting position of the eye, $\mathbf{R}_{head\ angle}$ accounts for head direction relative to maze coordinate, and $\mathbf{T}_{head\ pos.}$ translates the origin from the center of the maze to the center of the head (all matrices are 4x4). Head position and angle were obtained from the mouse tracker, whereas the resting position of the eye was fixed to $\varphi = 60$ degrees (azimuth) and $\Theta = 10$ degrees (elevation; Oommen and Stahl, 2008), see Figure S2. The eyes were finally rotated from the resting position based on our measurements of stabilizing eye movements (vestibulo-ocular reflex, VOR; gain value = -0.3; see Figure 3E and Equation 19).

A point (**p**) in maze coordinates could thus be projected onto the retina by first transforming it into retinal coordinates and by subsequently checking where the resulting vector intersects the retinal surface. This method allowed us to determine the stimulus area on the retina by projecting multiple points along the stimulus contour. It was, however, inconvenient to find the rods influenced by the stimulus in this way. We therefore used the inverse transform $\mathbf{M}^{-1}$ for transforming rod positions on the retina to maze coordinate, and then checking where the resulting vectors intersected the stimulus plane. Rods that intersected the plane within the stimulus were considered to be under the stimulus, and so also the RGCs that received input from these rods.

Ideal observer model

We used an ideal observer model for correlating the responses of populations of ON-S or OFF-S RGCs with behavioral data. This ideal observer had access to the spike trains of the entire RGC population (ON-S or OFF-S RGCs) throughout the full swimming trajectory of each mouse used for behavioral experiments. In addition, the ideal observer performed perfect path integration (so as to correlate RGC spike trains perfectly with the outside world coordinate system). To match the model performance with the WT mouse behavioral data, we created less ideal and thus more realistic versions of the original ideal observer by giving it a finite memory component defined by a single parameter. Below we explain in detail the structure of the ideal observer model and its rationale.

Initially, the maze circumference was divided up into n regions $[s_1,\ s_2,\ \ldots,\ s_n]$ (Figure S7A). Each region represents one possible stimulus locations, and each region is projected onto m ON-S or OFF-S RGCs on the retina (Figure S7B). We used n = 60 ($\sim$maze circumference divided by stimulus diameter) and $m = 5$ ($\sim$the number of ON-S or OFF-S spatial receptive fields (RFs) partially covered by the real stimulus, when the RF radius is taken as one σ). The identities of the RGCs that a specific region projects onto vary as the mouse swims around, but we assume that the ideal observer can account for this through path integration: the "ideal" mouse has control over its own movements and knows how much it has moved its head relative to a previous position. So, for each time bin, we extract the spikes of those RGCs that would respond to a stimulus within each region. We thus obtain 2n (both retinas) region-specific matrices that contain the spike counts of each region's m responding RGCs in every time bin (Figure S7C). Finally, the two matrices corresponding to the same region in the two eyes are concatenated and the resulting matrix vectorized. The ideal observer thus faces a task where it has to make an optimal choice among n vectors: one signal vector ($\mathbf{x}_{signal}$) representing the region of the actual stimulus, and n - 1 noise vectors ($\mathbf{x}_{noise}$) representing all the other possible regions. The elements of both vector types are stochastic (they represent spike counts subject to random variation), and their difference lies in the distributions that the elements are drawn from. All elements of $\mathbf{x}_{noise}$ are drawn from a Poisson distribution (RGCs are modeled using an LNP model) with a mean corresponding to the average baseline firing rate of the RGC type (not driven by the stimulus), whereas the elements of $\mathbf{x}_{signal}$ are drawn from Poisson distributions with mean rates given by predicted cell responses to the stimulus. For a linear classifier, the selection problem can be formulated as searching for a vector $\mathbf{w}$ that optimizes the separability of the dot products $\mathbf{w}^T\mathbf{x}_{noise}$ and $\mathbf{w}^T\mathbf{x}_{signal}$. Like Chichilnisky and Rieke (2005), we sought to maximize the distance between the means of the distributions for $\mathbf{w}^T\mathbf{x}_{noise}$ and $\mathbf{w}^T\mathbf{x}_{signal}$, or equivalently, to maximize the dot product $\mathbf{w}^T(\mu_{signal} - \mu_{noise})$. In our case, however, μ_{signal} is not known, as it depends on the stimulus intensity used and on the relative position of the mouse to the stimulus. This makes the classification task more challenging, but we can still restrict the region that μ_{signal} might vary within. Our estimated temporal filters are highly monophasic (Figure 4D), indicating that each element of μ_{signal} will always be larger than μ_{noise} for ON-S RGCs and smaller than μ_{noise} for OFF-S RGCs. For ON-S RGCs, we can thus instead maximize the expected distance between $\mathbf{w}^T\mu_{noise}$ and $\mathbf{w}^T\mu_{signal}$:

$$\max E\left[\mathbf{w}^{T}\left(\mathbf{\mu}_{\text{signal}} - \mathbf{\mu}_{\text{noise}}\right)\right] = \max \int_{D_{\text{ON}}} \text{p}\left(\mathbf{\mu}_{\text{signal}}\right)\mathbf{w}^{T}\left(\mathbf{\mu}_{\text{signal}} - \mathbf{\mu}_{\text{noise}}\right)d\mathbf{\mu}_{\text{signal}}, \text{ subject to } \mathbf{w}^{T}\mathbf{w} = c^{2}, \tag{11}$$

where D_{ON} denotes the domain of integration, $\text{p}(\mathbf{\mu}_{\text{signal}})$ denotes the probability of $\mathbf{\mu}_{\text{signal}}$ occurring, and c is an arbitrary constant. Using the method of Lagrange multipliers, we find that the Lagrangian is:

$$L(\mathbf{w},\ \lambda) = \int_{D_{\text{ON}}} \text{p}\left(\mathbf{\mu}_{\text{signal}}\right)\mathbf{w}^{T}\left(\mathbf{\mu}_{\text{signal}} - \mathbf{\mu}_{\text{noise}}\right)d\mathbf{\mu}_{\text{signal}} - \lambda\left(\mathbf{w}^{T}\mathbf{w} - c^{2}\right), \tag{12}$$

with the partial derivatives:

$$\frac{\partial L}{\partial \mathbf{w}} = \int_{D_{\text{ON}}} \text{p}\left(\mathbf{\mu}_{\text{signal}}\right)\left(\mathbf{\mu}_{\text{signal}} - \mathbf{\mu}_{\text{noise}}\right)d\mathbf{\mu}_{\text{signal}} - 2\lambda\mathbf{w}, \tag{13}$$

$$\frac{\partial L}{\partial \lambda} = \mathbf{w}^{T}\mathbf{w} - c^{2}. \tag{14}$$

The partial derivative for $\mathbf{w}$ can be simplified further by assuming that all values between the baseline and the maximum spike count (μ_{max}) are equally likely for each element of $\mathbf{\mu}_{\text{signal}}$. In which case, the integral simplifies to $((\mu_{\text{max}} - \mu_{\text{noise}})\mathbf{1}/2)$, and the condition for a stationary point becomes:

$$\frac{\partial L}{\partial \mathbf{w}} = 0 \Rightarrow \mathbf{w} = \frac{(\mu_{\text{max}} - \mu_{\text{noise}})\mathbf{1}}{4\lambda}. \tag{15}$$

The optimal vector $\mathbf{w}$ is thus some scalar multiplied by a vector of ones. The scalar is arbitrary, it only adjusts the magnitude of $\mathbf{w}$, and for simplicity, we set it to unity so that $\mathbf{w}$ simply is a vector of ones. The dot products $\mathbf{w}^{T}\mathbf{x}_{\text{noise}}$ and $\mathbf{w}^{T}\mathbf{x}_{\text{signal}}$ then get an interpretable meaning, as they sum the spike counts in $\mathbf{x}_{\text{noise}}$ and $\mathbf{x}_{\text{signal}}$, that is, the vector $\mathbf{w}$ that maximizes the expected distance between the means simply counts spikes. The derived ON-S ideal observer should thus select the region s whose cells have fired the most spikes, and we can explicitly calculate the probability for this being the right choice: $\mathbf{w}^{T}\mathbf{x}_{\text{noise}}$ and $\mathbf{w}^{T}\mathbf{x}_{\text{signal}}$ are both Poisson distributed, they only sum the independent Poisson distributed spike counts of the LNP modeled RGCs ($\mathbf{w} = \mathbf{1}$), and we thus find the probability for selecting the true stimulus region among $n-1$ incorrect regions as:

$$p_{\text{correct}} = \sum_{j=1}^{\infty} p\left(\mathbf{1}^{T}\mathbf{x}_{\text{signal}} = j\right)\left(\sum_{k=0}^{j-1} p\left(\mathbf{1}^{T}\mathbf{x}_{\text{noise}} = k\right)\right)^{n-1} \tag{16}$$

where $\text{p}()$ denotes Poisson distributions. Calculating p_{correct} from $\mathbf{w}^{T}\mathbf{x}_{\text{signal}}$ directly does, however, imply that the ideal observer gathers evidence during the whole swimming trajectory. This represents the ultimate optimum, but we also created constrained versions of the ideal observer that had a memory of T time steps (making the ideal observer less ideal). In practice, this meant that we 1) cross-correlated each spike count matrix with a vector of T ones, 2) summed the resulting matrix horizontally, and 3) calculated p_{correct} at each time point separately. The final result was then taken to be the maximal value of p_{correct} observed, from the start to 1 s before entering the first arm of the maze (p_{correct} grew rapidly once the mouse started swimming toward the stimulus). The ideal observer for OFF-S cells can be derived in an equivalent manner, and it was implemented in an identical way with the only difference being that it chose the region with the fewest spikes.

Standard errors for our ideal observers were obtained by creating multiple versions. Each version with LNP modeled RGC whose fixed sensitivity was sampled from the distribution of 2AFC measurements.

Data analysis

All data analyses were carried out using MATLAB (version: R2016a) and the publication figures were assembled using Origin (version 2018b).

Rod single-photon response amplitude and collecting area

Rod data were digitally low-pass filtered at 20Hz before data analysis. The amplitude of the single-photon response was estimated from the mean and the time-dependent ensemble variance of responses to a sequence of identical dim-flashes as previously described (Rieke, 2000; Ala-Laurila et al., 2007). Briefly, the square of the mean response $\bar{r}^{2}(t)$ for dim flashes is proportional to the ensemble variance of the response $\sigma^{2}(t)$ according to $\bar{r}^{2}(t) = \bar{n}\sigma^{2}(t)$, where the scalar $\bar{n}$ is the expected number of R* per flash and t is time. We estimated $\bar{n}$ by scaling $\sigma^{2}(t)$ to match $\bar{r}^{2}(t)$. Thus, the single-photon response, $\hat{r}(t) = \bar{r}(t) / \bar{n}$. Rod collecting areas at the wavelength corresponding to peak sensitivity (~500 nm) were obtained by first converting the LED output to equivalent photons at 500 nm (i.e., to the 500-nm photon density producing the same number of R*s in the rod, as previously described Azevedo and Rieke, 2011). Then the isomerization rate obtained from the variance analysis was divided by the equivalent photon density at 500 nm to obtain peak collecting areas for rods (A_{c} μm^{-2}): 0.63 ± 0.078 (WT, n = 20 rods); 0.41 ± 0.046 (OPN, n = 24 rods). No correction was

made for the transverse stimulation (rod recordings) versus axial stimulation (RGC and behavioral recordings), since the correction was calculated to impact A_c estimates of mouse rods less than 20%, which was within other factors of uncertainty (for details, see Lyubarsky et al., 2004). For this calculation the following assumptions were made: rod length = 24 μm, rod diameter = 1.4 μm, and the specific optical density of rhodopsin = 0.019 o.d. units/μm (Lyubarsky et al., 2004; Carter-Dawson and LaVail, 1979; Cornwall et al., 2000).

L-cone pigment content estimates

The amount of L-cone pigment in the rod was estimated as previously described (Fu et al., 2008). First, the spectral sensitivity of the rod for three different LEDs with peaks at 590 nm, 660 nm and 740 nm were determined using previously described methods (Ala-Laurila et al., 2007). Briefly, we fitted intensity-response series taken at reference LED (590-nm LED) with the Michaelis equation: $r = R_{max} \cdot I / (I + I_s)$, where r is the response amplitude (pA), R_{max} is the maximum dark current (pA), I is the flash intensity (photons μm^{-2}) and I_s is the half-saturating flash intensity (photons μm^{-2}). We fitted this equation by using I_s as a free parameter to the mean amplitude of the interleaved responses taken with test LEDs (660-nm and 740-nm LEDs) between two intensity-response families taken at the reference wavelengths (590-nm LED). The relative sensitivity for the two LEDs (rS) was defined as $rS = I_{s,ref} / I_s$, where $I_{s,\,ref}$ is the half-saturating flash intensity with the reference LED. The relative sensitivities (rS) were averaged over cells for OPN and WT. The logarithm of the ratio of the means, log (rS (OPN) / rS (WT)), was calculated. The L-opsin pigment content in the OPN mouse was estimated by choosing the fraction of the L-opsin absorption spectrum that, by the least square fit, provided the best fit to the logarithmic ratio of means, log rS (OPN) / rS (WT) for both the 660-nm LED and the 740-nm LED. For the fitting procedure, we used a linear combination of rhodopsin and L-cone pigment templates (Govardovskii et al., 2000) with the wavelengths corresponding to the peak of the spectrum (λ_{max}) at 497 nm for rhodopsin and 557 nm for human L-cone pigment.

Discrimination performance for rods, and RGCs

To determine the absolute threshold for rods and RGCs, a two-alternative forced choice task (2AFC) was used as previously described (Ala-Laurila and Rieke, 2014). In brief, we computed the instantaneous firing rate of RGCs in 10-ms bins. The mean response over all the trials was used as the discriminant in both rod and RGC recordings. We computed the correlation between the discriminant and the signals in 400-ms (RGCs) and 500-ms (rods) intervals preceding and following the flash. We classified the flash detection as correct if the correlation with the response after the flash was larger than that with the response prior to the flash. If the correlation values were equal, half of the epochs were assigned as correct choices and half as incorrect choices corresponding to the forced-choice procedure. The absolute threshold was defined as the light intensity that corresponds to the mid-point (= 0.75) of the possible range. The 2AFC procedure automatically takes into account the differences in tonic firing rates. Furthermore, we tested the impact of the spontaneous firing rate on detection thresholds for OFF-S RGCs, since the firing rates of OPN OFF-S RGCs were higher (62 ± 3 Hz, n = 33 cells) than those of WT OFF-S RGCs (50 ± 2 Hz, n = 61 cells, mean ± SEM). There was no significant correlation between the 2AFC thresholds and the spontaneous firing rates for WT OFF-S RGCs (r^2 = 0.017, p = 0.32, F-test) or for OPN OFF-S RGCs (r^2 = 0.0072, p = 0.64, F-test).

Analysis of the probability of finding all RGC types

Targeting all RGC types is not technically feasible in these recording conditions based on the soma sizes or other morphological characteristics. Furthermore, even multielectrode recordings would not offer unambiguous clustering of all RGC types in the mouse retina, and fluorescence targeting and/or other optical approaches would not be possible without impacting the RGC sensitivities in darkness. We therefore took a probabilistic approach, where we first targeted ON-S or OFF-S alpha RGCs in a particular retinal mount, and subsequently recorded from all other neighboring RGCs in the RGC mosaic. The probability of finding one or more RGCs of a particular type P_i was determined as $P_i = 1 - (1 - p_i)^N$, where N is the total number of other RGCs targeted and p_i is the probability of randomly selecting an RGC of type i. The probabilities p_i were based upon the reported group percentages of 32 groups (types) in Baden et al., 2016, The probability of finding n out of the 30 "other" RGC types (other than ON-S or OFF-S alpha RGCs) was determined by repeatedly drawing random samples from a cell type distribution based on the p_i values, and by averaging the number of found cell types over many trials. Our final probability estimates are nonetheless likely to be slightly underestimated, as the regular cell mosaic of each cell type is independent (Wässle and Boycott, 1991), and as the probability of finding one or more cells of the same type is higher than $1 - (1 - p_i)^N$ when sampling from neighbors. Even if there were more types than originally reported by Baden et al. (2016) this analysis gives a good framework to understand that our recordings covered most RGC types in the mouse retina.

Construction and validation of the LNP model

We represented ON-S and OFF-S RGCs with a time-space separable LNP model, where the linear filter was obtained from an outer-product between a temporal and a spatial filter, and where the nonlinearity resembled a rectified linear function, defined as:

$$f(z) = \begin{cases} \dfrac{e^z}{k}, & z < 0 \\[2mm] \dfrac{z+1}{k}, & z \geq 0 \end{cases} \tag{17}$$

The similarity score z constitutes a bias term (baseline firing rate) plus the cross-correlation between the filter and the stimulus, whereas the constant k was included to let the split in the nonlinearity occur at different locations relative to the baseline firing rate. We estimated filter parameters by minimizing the convex negative log-likelihood function:

$$-\ell = \sum_{i=1}^{N} f(z_i) - y_i \log f(z_i), \tag{18}$$

where y_i denotes the mean spike count in time bin i. For each cell, we obtained the temporal filter from responses to 16.7-ms (spot diameter: 200 μm) flashes at 3 to 5 different intensities. The negative log-likelihood was minimized for $k \in [0.125, 0.25, 0.5, \ldots, 128]$, where the k value with the lowest negative log-likelihood was selected. This step provided us with the shape of the temporal filter and a scaling that allowed us to predict responses at various intensities. The rectified nonlinearity obviously fails to capture the saturation effects of RGCs, but this does not matter as we are only interested in the initial parts of the intensity response curve (for very high firing rates it becomes trivial to detect the stimulus, see also Figure 4D). The spatial filter, in turn, was constrained to have the shape of a symmetric Gaussian, with sigma being the only free parameter. Sigma was extracted in a two-stage process from responses to 50-ms flashes presented at 30 different locations (triangular grid, 200 μm spot diameter; see Figure 4E inset). First, we estimated the full temporal (30 parameters, 0.5 s) and spatial filters (30 parameters) of a time-space separable LNP model by minimizing the negative log-likelihood (with additional L_2 regularization and cross-validation). This problem is non-convex, but it can be solved reliably by solving for the temporal and spatial parameters separately in an alternating fashion, as the subproblems are convex. Second, we found sigma through a least-square fit of a symmetric Gaussian to the full spatial filter. All LNP model parameters were thus estimated from brief flash stimuli only, and we evaluated the found parameters by predicting model responses to unseen test data consisting of flashes of previously unseen durations [33.3, 66.7, 133.3, 266.6] ms and a moving spot stimulus (200 μm spot moving across the spatial RF at 2000 μm/s; $\approx$ the median speed observed). We finally evaluated model predictions using the signal power explained (SPE, Sahani and Linden, 2003). This value is unbounded from below and bounded at 1 from above, and in contrast to commonly used correlation coefficients, it also takes scaling into account (Schoppe et al., 2016). Values close to unity thus mean that the predicted response occurs at the right time, that it has the right shape, and that it is scaled correctly (see Figure S6 for a comparison to other commonly used measures). The adequacy of the fixed nonlinearity was further evaluated by comparing measured intensity-response curves versus LNP model predictions (Figure 4D, right panel). The response was in all cases computed as the absolute deviation from the baseline firing rate, and thus reflected the mean number of additional or missing spikes in response to a flash.

Estimating the amount of compensatory eye movements

Compensatory eye-movements (vestibulo-ocular reflex (VOR)) were considered through a linear gain model. The model predicted the angular velocity of a compensatory eye-movement $\overline{v}_{eye}$ relative to the angular velocity of a head movement $\overline{v}_{head}$ around the yaw axis (axis orthogonal to the water surface):

$$\overline{v}_{eye} = g\overline{v}_{head}. \tag{19}$$

Average head and eye movement velocities were extracted from single head turn events, and the gain g was found through linear regression. The timing of eye and head movements was determined by calculating the cross-correlation over each complete head turn event as:

$$\text{cross corr.}(\tau) = \frac{\langle v_{eye}(t)v_{head}(t+\tau)\rangle - \langle v_{eye}(t)\rangle\langle v_{head}(t+\tau)\rangle}{\sqrt{\sigma_{eye}^2 \sigma_{head}^2}}, \tag{20}$$

where σ^2 denotes variance and the brackets time averages.

Fitting behavioral psychometric functions

We mapped the percentage of correct choices (entering the correct corridor as the first choice) as a function of stimulus intensity using a modified Hill function:

$$P_c(I) = P_{min} + (P_{max} - P_{min})\ \frac{I^n}{I^n + K^n}, \tag{21}$$

where P_c is the probability of finding the right arm, P_{min} is the chance level probability (= 1/6), P_{max} is the maximum probability (= 1.0), I is the stimulus intensity, K is the intensity at 58.3% correct choices, and n is the slope. Optimal K and n parameters were found by solving a joint least-squares problem, where each group (WT and OPN) had separate K parameters (separate thresholds) but shared n parameter (same slope). The identical slope made it possible to determine the shift in performance from the K parameters directly as K_{OPN}/K_{WT}. The Hill functions in Figure 3H where obtained by estimating K and n, as described above, to all data points in the low-intensity region ("Threshold region," < 1 R*/rod/s), as our emphasis was on the sensitivity threshold of vision.

Route histograms

The swimming trajectories of mouse population data (Figure 3H) were composed as a 2D histogram for each experimental condition. The visibility of low valued bins was enhanced by scaling the histograms with a gamma correction function p^γ, where p was the corresponding pixel value and γ was set to 0.5.

QUANTIFICATION AND STATISTICAL ANALYSIS

All error bars reported represent SEM. The normality of the data was tested using the Kolmogorov-Smirnov (KS) normality test. Student's t test (equal variances), Welch's t test (unequal variances), or one-way ANOVA (multiple groups) was used for normally distributed data. All t tests were two-tailed and two-sample unless otherwise noted. F-tests were used to test the equality of variances and datasets. A significance level of 0.05 was used in all statistical tests. The absolute threshold, flash sensitivity, and the ratios of these for RGCs are summarized as geometric mean and SEM. To determine whether two ratios of the absolute thresholds differ significantly, the t test was applied to the difference between the logarithms of the two ratios using the Welch-Satterthwaite equation to estimate the degree of freedom associated with the variance estimation.

DATA AND CODE AVAILABILITY

The datasets and code generated during the current study are available from the Lead Contact on request.